

1 **Comparison of commonly-used microwave radiative transfer models**
2 **for snow remote sensing**

3
4 Alain Royer^{a,b}, Alexandre Roy^{a,b}, Benoit Montpetit^{a*}, Olivier Saint-Jean-Rondeau^{a,b}, Ghislain
5 Picard^c, Ludovic Brucker^{d,e} and Alexandre Langlois^{a,b}

6 ^a Centre d'Applications et de Recherches en Télédétection (CARTEL), Université de Sherbrooke,
7 2500 boul. Université, Sherbrooke, QC, Canada, J1K 2R1.

8 ^b Centre d'Études Nordiques, Québec, Canada

9 ^c Université Grenoble Alpes - CNRS, LGGE UMR5183, 38041 Grenoble, France

10 ^d NASA Goddard Space Flight Center, Cryospheric Sciences Laboratory, Code 615, Greenbelt,
11 MD 20771, USA

12 ^e Universities Space Research Association, Goddard Earth Sciences Technology and Research,
13 Columbia, MD 21046, USA.

14 * Now at the Canadian Ice Service, Environment and Climate Change Canada, Ottawa.

15
16
17 **Abstract**

18 This paper reviews four commonly-used microwave radiative transfer models that take different
19 electromagnetic approaches to simulate snow brightness temperature (T_B): the Dense Media
20 Radiative Transfer – Multi-Layer model (DMRT-ML), the Dense Media Radiative Transfer –
21 Quasi-Crystalline Approximation Mie scattering of Sticky spheres (DMRT-QMS), the Helsinki
22 University of Technology n-Layers model (HUT-nlayers) and the Microwave Emission Model of
23 Layered Snowpacks (MEMLS). Using the same extensively measured physical snowpack
24 properties, we compared the simulated T_B at 11, 19 and 37 GHz from these four models. The
25 analysis focuses on the impact of using different types of measured snow microstructure metrics
26 in the simulations. In addition to density, snow microstructure is defined for each snow layer by

27 grain optical diameter (D_o) and stickiness for DMRT-ML and DMRT-QMS, mean grain
28 geometrical maximum extent (D_{max}) for HUT n-layers and the exponential correlation length for
29 MEMLS. These metrics were derived from either in-situ measurements of snow specific surface
30 area (SSA) or macrophotos of grain sizes (D_{max}), assuming non-sticky spheres for the DMRT
31 models. Simulated T_B sensitivity analysis using the same inputs shows relatively consistent T_B
32 behavior as a function of D_o and density variations for the vertical polarization (maximum
33 deviation of 18 K and 27 K, respectively), while some divergences appear in simulated variations
34 for the polarization ratio (PR). Comparisons with ground-based radiometric measurements show
35 that the simulations based on snow SSA measurements have to be scaled with a model-specific
36 factor of D_o in order to minimize the root mean square error (RMSE) between measured and
37 simulated T_B . Results using in-situ grain size measurements (SSA or D_{max} , depending on the
38 model) give a mean T_B RMSE (19 and 37 GHz) of the order of 16-26 K, which is similar for all
39 models when the snow microstructure metrics are scaled. However, the MEMLS model
40 converges to better results when driven by the correlation length estimated from in-situ SSA
41 measurements rather than D_{max} measurements. On a practical level, this paper shows that the SSA
42 parameter, a snow property that is easy to retrieve in-situ, appears to be the most relevant
43 parameter for characterizing snow microstructure, despite the need for a scaling factor.

44

45 **Keywords:** Snow microwave-emission model; Snow microstructure; Radiative transfer model;
46 Canada; Ground-based measurements; Brightness temperature

47

48

49 **1. Introduction**

50 In snow remote sensing, a better parameterization of the radiative transfer models (RTM) for
51 simulating snow microwave emission improves our ability to retrieve snowpack characteristics
52 from space-borne observations. Snow microstructure metrics are the main input parameter of the
53 microwave RTM (e.g. Rutter et al., 2009) and its characterization can strongly impact the
54 retrievals from microwave emission measurements for snow monitoring (e.g. Mätzler, 1994;
55 Armstrong and Brodzik, 2002; Kelly et al., 2003; Mätzler et al., 2006; Löwe and Picard, 2015).
56 Thus, given that the available models that are well-defined in the literature and commonly used
57 for snow remote sensing are defined by different snow microstructure parameterizations, a review
58 appears essential. We consider here the following four models: the Dense Media Radiative
59 Transfer– Multi layers (DMRT-ML) model (Picard et al., 2013), the Dense Radiative Transfer
60 Model – Quasi-Crystalline Approximation (QCA) Mie scattering of Sticky spheres (DMRT-
61 QMS) model (Chang et al., 2014), the multi-layer Helsinki University of Technology model
62 (HUT-nlayers) (Lemmetyinen et al., 2010a), and the Microwave Emission Model of Layered
63 Snowpacks (MEMLS) (Proksch et al., 2016; Wiesmann and Mätzler, 1999; Mätzler and
64 Wiesmann, 1999). Several aspects of these models are based on different electromagnetic
65 theories or semi-empirical approaches (multiple scattering and absorption coefficient
66 computations, for example), and they are often driven by sets of different measured inputs for
67 snow grain metrics, such as snow specific surface area (SSA), correlation length or snow grain
68 geometrical extent obtained from visual analysis.

69 Tedesco and Kim (2006) compared earlier simplified single-layer versions of the DMRT, HUT
70 and MEMLS models based on the snow grain metric given by visual inspection (average size
71 over the snowpack depth of representative small, medium, and large grains in each layer
72 measured using a microscope). MEMLS and HUT-nlayers were compared by Lemmetyinen et al.
73 (2010b) and Pan et al. (2016). DMRT theory and IBA were also recently compared and analyzed
74 (Löwe and Picard, 2015), while Roy et al. (2013) compared DMRT-ML and HUT-nlayers.

75 Sandells et al. (2016) compared DMRT-ML, HUT-nlayers and MEMLS models considering only
76 the optical diameter generated by snow models. But the four multi-layer models considered were
77 never compared together using coincident sets of measured snow properties. The main challenge
78 in comparing these RTM models is that the input snow microstructure parameters differ in each
79 model and are in some cases difficult or impossible to measure in the field. Three different snow
80 microstructure representations are considered in these models: optical diameter (D_o) and
81 stickiness for DMRT-ML and -QMS, correlation length (p_c) for MEMLS and maximum
82 geometrical extent (D_{max}) for HUT-nlayers. Consequently, some hypotheses are needed for their
83 estimation allowing coherent intercomparison of models (Löwe and Picard, 2015). For example,
84 it was previously shown that the optical diameter derived from the SSA needs to be scaled by a
85 factor in order to be in agreement with measurements when considering DMRT-ML with non-
86 sticky medium (Brucker et al. 2011; Roy et al., 2013; Montpetit et al., 2013; Picard et al. 2014;
87 Dupont et al., 2014). As the physical aspects of each model had already been extensively
88 analyzed, we put the emphasis in this paper on comparing the models with surface-based
89 measured brightness temperature (T_B). The objective is to compare the simulations using the
90 same in-situ measurements of improved snow parameterization, which had never been done.
91 This paper briefly recalls the main basic fundamentals of these four models and more specifically
92 the different grain size definitions involved (Section 2). After presenting datasets and snow
93 microstructure measurement methods (Section 3), we first compare the four models using a
94 synthetic snowpack to perform a sensitivity analysis (Section 4.1), and we then compare the
95 simulated T_B using sets of measured snow properties against measurements of surface-based
96 radiometric T_B at 11, 19 and 37 GHz (Section 4.3).

97

98 **2. Models and their respective snow microstructure metric**

99 A synthesis matrix of the four models considered in this study is presented in Table 1. These
100 models are all publicly available (thus specific details of their implementations can be known)

101 and are extensively described in the references given in Table 1. Readers are invited to consult
102 these references for detailed descriptions of the models, which are based on conceptually
103 different approaches for computing snow electromagnetic properties and radiation transfer in the
104 multi-layers of the snowpack. In this paper, all the simulations were performed using the
105 recommended configuration for DMRT-ML and -QMS, the Improved Born Approximation
106 (IBA) (option 12) for MEMLS and the original version of the extinction coefficient in HUT (see
107 Table 1).

108 One of the main difficulties in snow radiative transfer is the parameterization of snow
109 microstructure consisting of a high density of scatterers per unit of volume. DMRT-ML and –
110 QMS consider the snow as a collection of sticky spherical ice particles defined by their radius
111 and stickiness (Tsang and Kong, 2001; Tsang et al., 2007), while MEMLS parameterizes snow
112 microstructural properties by a second order statistical function, the two-point correlation
113 function, giving the mutual relationships between two scatterers within a given volume, such as
114 the autocorrelation function (the exponential correlation length p_{ex} is generally used, see Section
115 2.2 below). HUT is based on empirical scattering and extinction coefficients fitted with the
116 observed maximum dimension of snow grains (D_{max}), or more recently an effective grain size
117 radius (Kontu and Pulliainen, 2010). When using in-situ ground-based measurements of snow
118 microstructure parameterization, practical comparison of these models requires hypotheses to
119 retrieve and link the different metrics. The metrics used in this study are briefly defined below.

120

121 **Table 1** Comparison between basics of DMRT-ML/-QMS, MEMLS and HUT-nlayers models.

122 *See the Table at the end of the paper.*

123 **2.1 DMRT snow microstructure metric**

124 DMRT-ML considers snow grains as spherical particles of ice defined by their radius. Their
125 position (clustering) is controlled by stickiness. For snow having a wide range of grain shape, the
126 radius of equivalent spheres can be objectively defined by their optical radius (R_o), which can

127 always be derived from the SSA via the optical equivalent radius. The snow SSA is the surface of
 128 the air/snow interface (S) per unit of mass: $M = \rho_{\text{snow}} \cdot \text{Volume}$: $\text{SSA} = S/M = S/(\rho_{\text{ice}} \cdot \text{Volume})$ in m^2
 129 kg^{-1} , where ρ_{ice} is the ice density (917 kg m^{-3}). SSA measurements are described in Section 3. For
 130 spheres or snow assimilated as sphere equivalent (see the review paper by Domine et al., 2008),
 131 the optical radius (Ro) is expressed as (Ro in mm, ρ_{ice} in kg m^{-3} and SSA in $\text{m}^2 \text{ kg}^{-1}$):

$$132 \quad R_o = 3 \cdot 10^3 / (\rho_{\text{ice}} \cdot \text{SSA}) \quad (1).$$

133 Since any measurements can be used to estimate stickiness, Brucker et al. (2011), Roy et al.
 134 (2013), Dupont et al. (2014) and Picard et al. (2014), considering a non-sticky medium, have
 135 shown that Ro should be multiplied by the scaling factor ϕ_{DMRT} when Ro is derived from SSA
 136 measurements (R'o in mm):

$$137 \quad R'_o = \phi_{\text{DMRT}} R_o = 3 \cdot 10^3 \phi_{\text{DMRT}} / (\rho_{\text{ice}} \cdot \text{SSA}) \quad (2).$$

138 This scaling factor is discussed in Section 4.2. Roy et al. (2013) also showed that the following
 139 relationship (inspired by Kontu and Pulliainen, 2010) can be used for an effective optical radius
 140 of snow grains derived from SSA measurements:

$$141 \quad R''_o \text{ [mm]} = 1.1 [1 - \exp(-24.6 \cdot 10^3 / (\rho_{\text{ice}} \cdot \text{SSA})] \quad (3).$$

142 The stickiness parameter (τ), used by DMRT theory (Tsang and Kong, 2001), is inversely
 143 proportional to the contact adhesion between spheres. It can be linked to the cohesion or to a
 144 degree of connectivity between grains. Thus, for non-sticky spheres: $\tau = \infty$; for snow with
 145 clusters (aggregates) or grains with high strength of adhesion, τ decreases (for example $\tau = 1$ to
 146 0.2 or less). DMRT-ML uses the “short range” approximation (Tsang and Kong, 2001) which
 147 implies that grains and aggregates should remain small compared to the wavelength. Roy et al.,
 148 (2013) hypothesized that the needed scaling factor (ϕ_{DMRT}) is related to the assumption of non-
 149 sticky spheres ($\tau = \infty$) and to the assumption of monodisperse grain size distribution. This scaling
 150 factor is therefore a surrogate of the stickiness parameter which cannot practically be measured in
 151 the field (see Löwe and Picard, 2015).

152

153 **2.2 MEMLS snow microstructure metric**

154 MEMLS uses the correlation length (p_c) for describing snow microstructure, which is the slope of
155 the spatial autocorrelation function at the origin (i.e. the derivative of this function). This
156 parameter might be derived from micro-computed tomography measurements (micro-CT) (Löwe
157 et al., 2013) or by high-quality stereological method (see Riche et al., 2012), but its rapid
158 derivation from field measurements is still difficult. Recently, Proksch et al. (2015) proposed a
159 relationship between Snow-Micropen measurements and correlation length that has not yet been
160 validated for microwave emission applications.

161 Here, we first estimate the correlation length from the equivalent sphere grain radius (R_o) as
162 proposed by Mätzler (2002), following the Debye relationship:

$$163 \quad p_c = 4/3 R_o (1 - \nu) \quad (4),$$

164 where ν is the ice volume fraction: $\nu = \rho_{\text{snow}}/\rho_{\text{ice}}$.

165 While there is no experimental relationship between simultaneous measurements of p_c (from
166 micro-CT measurements) and SSA measurements, Montpetit et al. (2013) showed that the
167 following relationship gives optimized simulated T_B using MEMLS driven with SSA
168 measurements (p'_c in mm and SSA in $\text{m}^2 \text{kg}^{-1}$):

$$169 \quad p'_c [\text{mm}] = 4 \cdot 10^3 \phi_{\text{MEMLS}} (1 - \nu) / (\rho_{\text{ice}} \cdot \text{SSA}) \quad (5),$$

170 where ϕ_{MEMLS} is a scaling factor and SSA is measured in-situ.

171 If the autocorrelation function is approximated (fitted) by an exponential function of the form:
172 $\exp(-x/p_{\text{ex}})$, one can derive the exponential correlation length p_{ex} . According to the type of snow,
173 p_{ex} is different from p_c (Krol and Löwe, 2016; Mätzler, 2002). For microwave measurements, p_{ex}
174 is generally preferred to p_c , and Mätzler (2002) found in general that $p_{\text{ex}} \approx 0.75p_c$, giving from (1)
175 and (4):

$$176 \quad p_{\text{ex}} [\text{mm}] \approx R_o (1 - \nu) = 3 \cdot 10^3 (1 - \nu) / (\rho_{\text{ice}} \cdot \text{SSA}) \quad (6).$$

177 On the other hand, previous studies from Mätzler (1997) have shown that p_c is closer to the
178 minimum characteristic extent of the grain than related to the maximum geometrical particle
179 extent. Mätzler (2002) gives a series of measurements of p_c , p_{ex} and visually estimated grain size
180 D_{max} (defined below) for 20 samples of different snow types showing the correspondence
181 between these parameters. Using these data, p_{ex} (or p_c) can be expressed as a logarithmic function
182 of D_{max} :

$$\begin{aligned} 183 \quad p_{ex} &= a + b \ln(D_{max}) \quad \text{for } v > v_{th} \text{ and } D_{max} > D_{max,th} \text{ in mm} \\ 184 \quad p_{ex} &= C^{st} \quad \text{otherwise} \end{aligned} \quad (7),$$

185 where v_{th} and $D_{max,th}$ are thresholds delimitating the range of validity of the proposed model, and
186 C^{st} is a constant for values below these thresholds.

187 Using the Mätzler (2002) data, Durand et al. (2008) found that $a = 0.18$ and $b = 0.09$ for $v > 0.2$
188 and $D_{max} > 0.125$ mm, and that $p_{ex} = 0.05 \pm 0.017$ otherwise.

189

190 **2.3 HUT snow microstructure metric**

191 HUT input is based on individual grain size. There are many ways to describe the geometrical
192 grain size of snow (Colbeck et al., 1990; Lesaffre et al., 1998; Fierz et al., 2009). Among them,
193 one can cite the circle (or ellipsoid) that better encompasses the snow grain; the equivalent radius
194 given by the ratio between projected grain area and its perimeter; the mean convex radius of
195 curvature; or the greatest extent of the prevailing or characteristic grains: D_{max} . The latter
196 corresponds to the maximum dimension of the "intermediate grain size" and has long been a
197 classical parameter routinely used to visually characterize snow structure in the field (see
198 Colbeck et al., 1990; Fierz et al., 2009). The HUT model can be driven either directly by D_{max} , or
199 by an effective grain diameter ($D_{max,eff}$) derived from D_{max} following the relationship that
200 minimized the differences between measured and simulated T_B , as proposed by Kontu and
201 Pulliainen (2010) (see also Lemmetyinen et al., 2010a and 2015; Pan et al., [2016](#)):

202
$$D_{\max,\text{eff}} = 1.5 (1 - \exp(-1.5 D_{\max})) \quad (8),$$

203 where $D_{\max,\text{eff}}$ and D_{\max} are in mm.

204 However, in this study, it appears that this relationship (Eq. 8) for estimating the $D_{\max,\text{eff}}$ does not
205 give a good agreement, due to the lack of convergence in the optimization. This results from the
206 large digitized D_{\max} measurement values obtained in this study (see Section 4.2), and Eq. 8 leads
207 to a unique $D_{\max,\text{eff}}$. In the model comparison (Section 4.3), we thus consider $D_{\max,\text{eff}} = 0.5 D_{\max}$,
208 derived from an optimization that reduces the difference between simulated and measured T_B
209 (method of Roy et al., 2013).

210

211 When SSA is measured, Roy et al. (2013) use Equation (2), with a different scaling factor
212 (ϕ_{HUT}) relative to the effective grain size in HUT simulations:

213
$$D_{\text{eff}} [\text{mm}] = 6.10^3 \phi_{\text{HUT}} / (\rho_{\text{ice}} \cdot \text{SSA}) \quad (9).$$

214 All the ϕ factors (ϕ_{DMRT} , ϕ_{MEMLS} and ϕ_{HUT}) are further discussed in the results section. Field
215 measurement methods for SSA and D_{\max} estimates are presented in Section 3.

216

217 ***2.4 Scaling factors for the models driven by SSA measurements***

218 The scaling factor ϕ depends upon the model considered and the type of snow. The change in this
219 scaling factor is linked to other microstructure parameters such as stickiness and to the fact that
220 we assume a monodisperse size distribution of snow grain (see the discussions in Brucker et al.,
221 2011; Roy et al., 2013 and Löwe and Picard, 2015). It cannot be explained by measurement
222 uncertainties (Roy et al., 2016). Löwe and Picard (2015) theoretically demonstrate the need of
223 grain size scaling between the optical diameter and the equivalent sticky hard sphere diameter.
224 For DMRT-ML with the assumption of non-sticky spheres, the ϕ factor obtained varies from 2.3
225 to 3.5 depending on the type of snow (Table 2). The amplitude of this factor may also partly be
226 affected by errors in snow measurements and possibly in the soil parameters. Precise explanation

227 of these differences in the ϕ factor needs further study but is outside the scope of this paper. Here
 228 we used $\phi = 3.3, 1.3$ and 3.7 , respectively for DMRT-ML, MEMLS and HUT-nlayers (Table 2)
 229 in order to compare the known optimized models when driven by SSA measurements compared
 230 to simulations driven by D_{\max} measurements.

231
 232 **Table 2.** Scaling factor ϕ to be applied on the snow microstructure metric derived from in-situ
 233 SSA measurements, as a function of the RTM considered and the type of snow. All SSA
 234 measurements were derived from the DUFISSS's type approach (see Section 3.1), except *: the
 235 values depend upon the method used for retrieving SSA; and **: SSA retrieved from ASSAP
 236 device (see [details in the given references, last column](#)).

Radiative Transfer Models	Snow μstructure Metrics	Sites	ϕ	References
MEMLS	$p'_c=4.10^3 \phi (1 - \nu)/(\rho_{ice} \cdot SSA)$ Eq. 5	Canada: Arctic, Subarctic, South Québec	1.3	Montpetit et al., 2013
DMRT-ML (no stickiness)	$R'o=3.10^3 \phi /(\rho_{ice} \cdot SSA)$ Eq. 2	Dome C Antarctica	1.89, 2.5, 2.85*	Brucker et al., 2011
		Dome C Antarctica	2.3**	Picard et al., 2014
		Barnes Ice Cap Canada Arctic	3.5	Dupont et al., 2014
		Canada: Arctic, Subarctic, South Québec	3.3	Roy et al., 2013
HUT-nlayers	$R_{o_{eff}}=3.10^3 \phi /(\rho_{ice} \cdot SSA)$ Eq. 9	Canada: Arctic, Subarctic, South Québec	3.7	Roy et al., 2013

237

238 **2.5 Radiative Transfer Model inputs**

239 Apart from the snow microstructure parameterization, all other input parameters required by the
 240 four models are the same for each layer defined by its thickness, snow temperature and density.
 241 Here, we only considered dry snow. An important contribution to snowpack emission can
 242 emanate from the soil under the snowpack, in particular at low frequencies. For the
 243 intercomparison in this study, we thus used the same rough soil reflectivity model proposed by
 244 Wegmüller and Mätzler (1999) (see the review of Montpetit et al., 2015a). At a given frequency,
 245 the soil parameterization is defined by the soil/snow interface reflectivity in horizontal
 246 polarization (Γ_H) and vertical polarization (Γ_V) with the following equations for an incidence
 247 angle (θ) lower than 60° :

$$\Gamma_H = \Gamma_H^{Fresnel} \exp\left(- (k\sigma)^{\sqrt{-0.1\cos\theta}}\right) \quad (10),$$

$$\Gamma_V = \Gamma_H \cos\theta^\beta$$

250 where k is the incident medium wave number (air or snow), $\Gamma_H^{Fresnel}$ is the Fresnel reflectivity
 251 function which depends on the soil permittivity (ϵ_{soil}), σ is the soil roughness parameter and β is a
 252 scaling factor for deriving the reflectivity at vertical polarization from the computed reflectivity
 253 at horizontal polarization. Following Montpetit et al. (2015b), we consider the optimized values
 254 of ϵ_{soil}^{eff} , σ^{eff} and β^{eff} parameters for each frequency given in Table 3.

255

256 **Table 3.** Soil parameters considered for the three models (see Eq. 10).

Frequency (GHz)	ϵ_{soil}^{eff}	β^{eff}	σ^{eff} (cm)
11	3.18-0.006134j	1.08	0.19
19	3.42-0.00508j	0.72	
37	4.47-0.32643j	0.42	

257

258 For comparisons between simulated T_B and measurements, the downwelling sky radiance
 259 reflected by the snowpack toward the radiometer has to be taken into account ([Montpetit et al.](#),

260 | [2013; Courtemanche et al., 2015; Roy et al., 2016](#)). In each surface-based radiometric
261 | measurement, the atmospheric contribution was calculated using the atmospheric Millimeter-
262 | wave Propagation Model (MPM: Liebe, 1989) implemented in the HUT snow emission model
263 | (Pulliainen et al., 1999). The atmospheric model was driven with the air temperature and
264 | precipitable water of the atmospheric layers above the surface given by the 29 atmospheric layers
265 | of the North American Regional Reanalysis ([NARR](#)) (Mesinger et al., 2006) for the [NARR](#) pixel
266 | and [time](#) of measurements. Note that all the snowpits were located in open areas where no
267 | vegetation could contribute to the measured T_B ([see the discussion in Roy et al., 2016](#)). [We](#)
268 | [previously validated this procedure against sky microwave measurements \(see Courtemanche et](#)
269 | [al., 2015\)](#).

270

271 | **3. Ground-based measurement dataset**

272

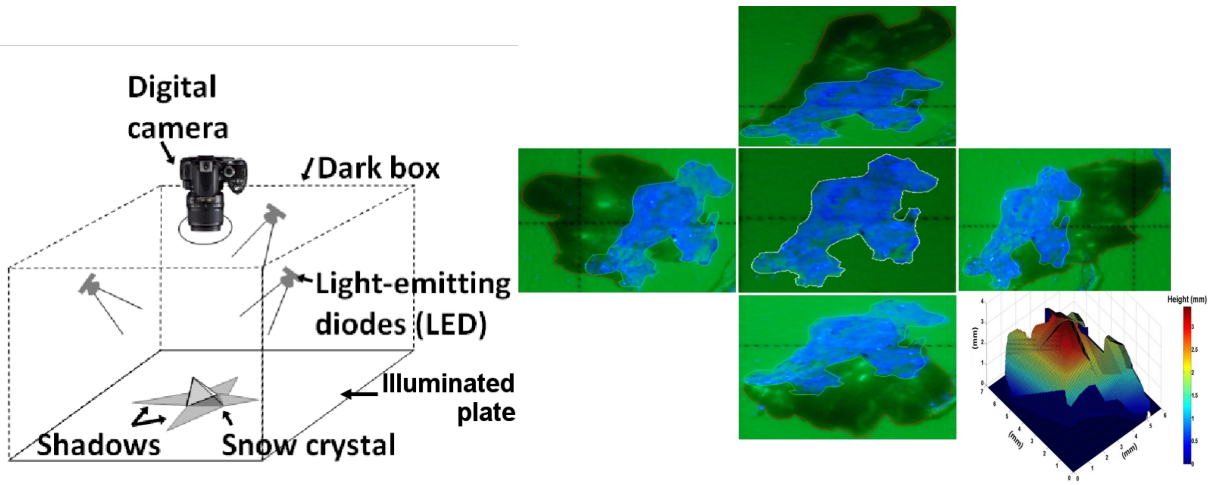
273 | ***3.1 Optical radius retrieved from SSA measurements using IRIS***

274 | A light short-wave infrared laser-based system measuring snow albedo through an integrating
275 | sphere (InfraRed Integrating Sphere, IRIS), similar to the system previously proposed by Gallet
276 | et al. (2009), was used for SSA measurements (Montpetit et al., 2012). Relatively good accuracy
277 | (12-15%) and reproducibility in SSA measurements are obtained using the IRIS system on
278 | extracted samples. Gallet et al. (2009) and Montpetit et al. (2012) describe in detail these devices
279 | (Dual Frequency Integrating Sphere for Snow SSA: DUFISSS and IRIS, respectively).
280 | Lambertian targets with known reflectance values (Spectralon: 0.06, 0.25, 0.60, 0.79, and 0.98 at
281 | 1.33 μm) were used to calibrate the device before and after each series of measurements at each
282 | site. From the reflectance, the SSA was calculated as described by Montpetit et al. (2012). SSA
283 | measurements allow us to estimate the mean optical radius of grain sizes of each layer (Eq.1),
284 | assuming that all grains have the same size (monodisperse size distribution).

285

286 3.2 D_{max} measurements using multidirectional lighting macrophotos in the Shadow-box

287 Macrophotos of snow grain samples have been widely used in numerous studies (e.g. Colbeck,
288 1990; Fierz et al., 2009). In order to improve geometrical snow grain parameterization, we
289 developed an optical system that uses, within an enclosed box (30x30x30 cm), five light-emitting
290 diodes that provide five-direction (nadir, N, E, S and W) illumination of a gridded plate upon
291 which snow grains are placed (Fig. 1). Five photographs are taken successively for each
292 illuminated direction with a Nikon D40 fitted with a macro lens (Fig. 1). The projected area of
293 the grain is extracted from a first photograph with the diode illuminating from nadir and the four
294 other photographs allow the digitization of the projected shadows. Knowing the angles of
295 illumination and the exact position of each grain on the gridded illuminated plate, it is possible to
296 calculate the height of the grain envelope using the tangent illumination path corresponding to the
297 projected shadow in each direction. We thus derived a numerical height model of each snow
298 grain and reconstructed a 3D representation of the snow grain envelope (Fig. 1). From this
299 elevation model, one can derive multiple size parameters: D_{max} , minor and major axis of the
300 envelope ellipsoid, projected area, mean height, maximum height and apparent volume and
301 surface area. All of these parameters are then averaged for each sample. This device (called
302 *Shadow-box*) is very easy to handle in the field, and improves the retrieval of a 3D representation
303 of the snow grains. It is also useful to characterize snow grain shapes and types of extracted snow
304 samples. Using calibrated spheres (steel balls from 0.8 to 4.8 mm), the retrieval error (bias) on
305 D_{max} was estimated of the order of 0.03 mm. The measurement protocol is as follows: we gently
306 cover the plate with separated grains of a snow sample extracted from each snowpack layer
307 (approximately every 3 cm over the snowpit), and take the five consecutive macrophotos,
308 including identifications of the snowpit and layer. We then systematically manually digitize the
309 contour of all the grains on the plate to estimate the mean D_{max} (2D) values for each snowpack
310 layer. The shadows help to discriminate individual grains in aggregates or when grains are stuck
311 together.



312
313

314 **Fig. 1** Shadow-box. Snow grains placed on the plate are successively illuminated from four
315 directions by four LEDs and by one LED from the nadir, producing five macrophotos (right),
316 from which a 3D envelope model of the grain can be retrieved after manual digitization of the
317 shadows. The size of the grain shown is 7 mm.

318

319 **3.3 Correlation length**

320 Since no direct measurement of correlation length was carried out, the values of correlation
321 length (p_c or p_{ex}) used as inputs for MEMLS were estimated in three ways: (1) from the retrieved
322 optical grain size radius (SSA measurements) and the fractional volume (Debye relationship, Eq.
323 5) (hereafter labeled MEMLS_Do); (2) from the measured values of mean D_{max} grain size (2D
324 Shadow-box) and fractional volume based on the Mätzler relationship (Durand et al., 2008)
325 (hereafter labeled MEMLS_ D_{max_pex}); and (3) from p_{ex} based on the observed linear relationship
326 between p_c and D_{max} shown in the results section (see Fig. 5) (hereafter labeled
327 MEMLS_ D_{max_lin}).

328

329 **3.4 T_B measurements**

330 T_B measurements were taken for every snowpit at 10.67 (hereafter noted 11), 19 and 37 GHz in
331 vertical polarization (V-pol) and horizontal polarization (H-pol) at a height of approximately 2 m

332 above the surface using PR-series field radiometers (Radiometrics Corporation, Boulder, CO,
333 USA) at an incidence angle of 54°-55°, which is close to the measurement incidence angle of the
334 Advanced Microwave Scanning Radiometer – Earth Observing System (AMSR-E) and Special
335 Sensor Microwave Imager (SSM/I) space-based sensors. The ellipsoidal footprint of
336 measurements at the snow surface was approximately 0.5 m × 0.65 m. The radiometer calibration
337 was based on two measurements taken with the absorbing foam Eccosorb© (Cuming Microwave
338 Corporation, MA, USA) at the ambient temperature (i.e. warm reference) and another taken over
339 a surface of liquid nitrogen (i.e. cold reference) (Asmus and Grant, 1999; Langlois, 2015). In the
340 worst case, measurement error for the calibration target was estimated at ±2 K. Ambient and cold
341 point measurements from before and after the field campaign periods (typically separated by five
342 to ten days) were used to produce a final calibrated T_B data set.

343

344 ***3.5 In-situ snow data***

345 The snow data needed by the models were derived from in-situ measurements in three northern
346 Canadian regions. Table 4 provides the data from the Arctic: Churchill (MB), the Subarctic
347 region: James Bay (QC), and southern regions of Québec: Sherbrooke (QC) and St-Romain
348 (QC). All sites were already well-described in the references given in the Table 4. This database
349 of 32 snowpits encompasses a wide range of snow types (i.e. metamorphic processes and
350 stratigraphy), typical of North American environments. For each site, profiles of snow
351 temperature, snow density, and snow microstructure were taken at a vertical resolution of 3 or 5
352 cm in the footprint of the microwave radiometers. The density was measured with a 185 cm³
353 density cutter, and the samples were weighed with a 100 g Pesola light series scale with an
354 accuracy value of 1 g. The temperature was measured with a Traceable 2000 digital temperature
355 probe (±0.1°C). The microstructure of each layer was defined with both SSA (optical radius) and
356 D_{max} measurements, the latter using macrophotos (Shadow-box). In Table 4, we give the
357 vertically averaged values of density, optical radius and D_{max} , weighted by the snow layer

358 | thicknesses and the derived bulk p'_c (from Eq. 5) were also estimated (9th column). The
359 | stratigraphy was examined at each site, and all ice lenses (or crusts), when present, were
360 | identified and measured. Their density was not measured as this is very difficult to properly
361 | sample. All the microwave and snow measurements were always synchronised in time. All these
362 | 32 sites (Table 4) were used for model comparison.

363 |
364 | **Table 4.** Summary of the snow parameters of all sites analyzed in this study. Site name: CHxx
365 | corresponds to Churchill, MB sites (Roy et al., 2013; Montpetit et al., 2013); SIRSP4 and RoSP1
366 | correspond to the southern Québec sites, respectively to the SIRENE site at Sherbrooke, QC and
367 | to the St-Romain, QC site (Roy et al., 2013); BJxx sites corresponds to the James Bay, Nunavik,
368 | QC sites (Subarctic sites) (Roy et al., 2016). The snowpits where an ice lens was observed are
369 | identified (last column).

	Site Name	Snow depth (m)	Tsnow (K)	Density (kg/m ³)	Tsoil (K)	Optical radius (mm)	Dmax (mm)	Bulk p'_c (Eq. 5)	Ice lens
1	CH42	0.37	259.4	289.4	267.9	0.22	4.43	0.267	
2	CH43	0.70	257.3	311.4	270.3	0.20	2.68	0.231	
3	CH83	1.18	269.4	372.6	272.7	0.19	2.83	0.199	
4	CH90	0.82	265.3	284.0	271.8	0.18	3.43	0.213	
5	CH91	0.91	267.1	324.7	272.5	0.19	4.16	0.210	
6	CH92	0.83	268.3	292.8	272.9	0.22	3.10	0.262	
7	CH95	1.74	266.0	380.3	272.8	0.15	1.89	0.150	
8	CH96	1.80	266.8	367.8	272.9	0.17	2.20	0.172	
9	CH97	1.50	266.4	380.9	272.7	0.18	2.07	0.178	
10	CH98	1.19	265.8	351.4	272.5	0.16	2.04	0.166	
11	CH104	0.48	255.2	261.4	269.6	0.32	4.90	0.393	
12	CH105	0.45	258.7	229.7	270.3	0.32	6.11	0.419	
13	CH111	0.44	252.5	284.6	269.8	0.25	4.54	0.303	
14	CH55	0.51	258.5	308.4	269.7	0.19	3.54	0.214	
15	CH56	0.35	254.9	314.6	267.2	0.20	3.15	0.231	
16	CH99	0.57	259.3	328.0	270.1	0.23	4.02	0.255	
17	CH101	0.19	259.1	263.2	264.6	0.33	4.88	0.403	
18	CH54	0.48	257.1	345.0	269.5	0.20	4.51	0.215	x
19	CH57	0.25	260.2	321.9	266.1	0.20	3.50	0.224	
20	CH58	0.35	256.5	304.6	267.9	0.16	4.84	0.189	x
21	CH59	0.65	260.2	276.6	271.7	0.23	3.71	0.274	x
22	CH60	0.14	270.4	288.3	262.2	0.27	3.83	0.325	x
23	CH61	1.03	260.5	400.8	272.5	0.19	2.68	0.187	
24	CH82	0.35	266.5	285.4	270.8	0.37	4.08	0.446	
25	CH93	0.82	279.6	311.9	271.9	0.28	4.43	0.325	x

26	CH100	0.43	259.8	295.8	269.2	0.28	4.78	0.328	x
27	CH114	0.72	283.2	323.0	272.8	0.33	3.19	0.373	x
28	CH115	0.31	271.4	313.6	272.2	0.33	5.11	0.382	
29	SIRSP4	0.33	271.5	245.9	273.0	0.14	3.07	0.173	
30	RoSP1	0.47	269.4	179.2	273.5	0.08	1.05	0.107	x
31	BJjan1	0.51	266.8	284.9	271.5	0.16	3.07	0.191	x
32	BJfev2	0.66	265.8	245.1	273.1	0.18	2.01	0.229	x

370

371

372 4. Results

373

374 A sensitivity analysis is first performed to compare the four models considered with the same
375 inputs considering a synthetic snowpack (Section 4.1). We then discuss the consistency between
376 the grain size measurements (Section 4.2), and we compare the simulations with ground-based
377 measurements (Section 4.3).

378

379 4.1 Sensitivity analysis of the three models

380 Based on an identical synthetic snowpack, we seek to illustrate model sensitivity to three
381 parameters: - grain size (Fig. 2); - density (Fig. 3); - and ice lens in the snowpack (Fig. 4).

382 Fig. 2 shows the comparison between the 37 GHz brightness temperature variations as a function
383 of D_0 , using the four models in a very simple synthetic case defined by one layer of 1 m

384 thickness with a mean uniform density of 250 kg m^{-3} . The incidence angle of T_B simulations is
385 55° . All input parameters were the same for the four models and the different microstructure
386 metrics were derived from the same initial grain parameter (D_0) using equations (2), (5) and (9).

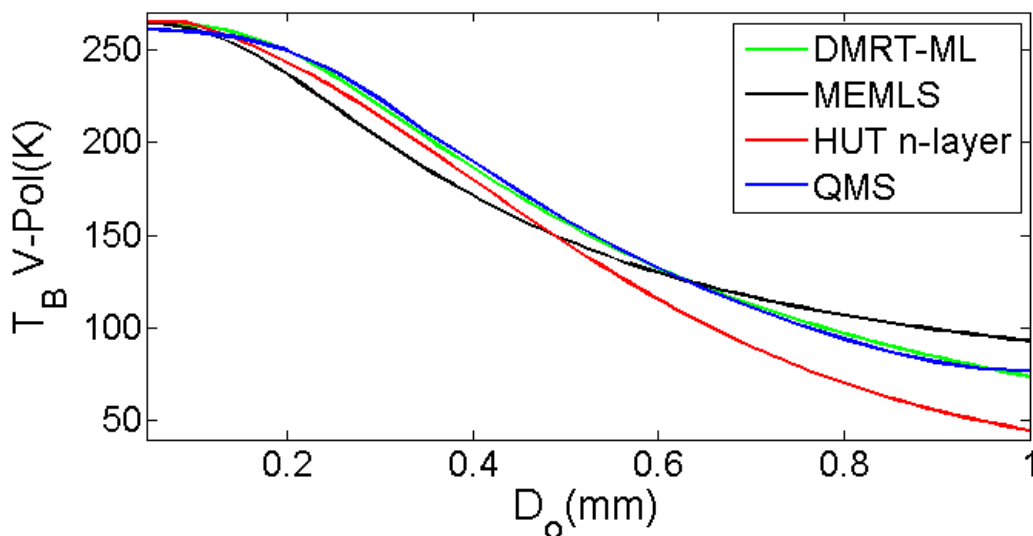
387 To define the optical diameter of each model, we used the scaled factors defined in previous
388 analysis (see discussion in Section 4.2). These factors optimize the simulations compared to in-
389 situ radiometric measurements for real snowpacks. The relationships defining the microstructure

390 metrics were derived from Equations (2), (5) and (9), respectively for DMRT-ML (assuming
391 non-sticky spheres) (Roy et al., 2013), MEMLS-IBA (Montpetit et al., 2013) and HUT (Roy et

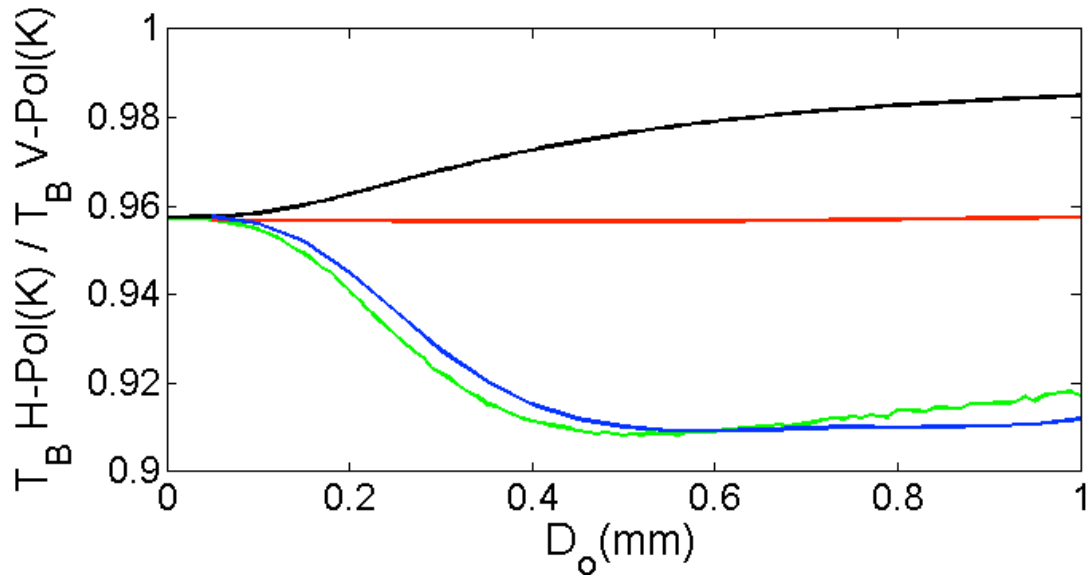
392 al., 2013). For DMRT-QMS, we used the same relationship as for DMRT-ML, and also assuming
 393 non-sticky spheres. The comparison in Fig. 2 is thus performed using the following equations:

$$\begin{cases}
 394 \text{ DMRT-ML/-QMS: } D'o = 3.3 D_o \\
 395 \text{ MEMLS: } p'_c = 1.3 (2/3) D_o (1-\nu) \\
 396 \text{ HUT: } D_{o_{\text{eff}}} = 3.7 D_o
 \end{cases} \quad (11)$$

397 The results show that the T_B simulated by the four models similarly decrease with the grain size,
 398 as expected due to the high sensitivity of microwave attenuation to grain size at 37 GHz. Using
 399 the scaling factors for the input grain size metrics given in Eq. 11, the simulated T_B V-pol are
 400 close for D_o around 0.5 mm and for $D_o < 0.2$ (Fig. 2, top). However, MEMLS T_B values appear
 401 underestimated by 18 K compared to DMRT-ML/-QMS around $D_o = 0.3$ mm. Note that DMRT-
 402 ML is identical to DMRT-QMS over the whole analyzed range of D_o , as we stay in the Rayleigh
 403 range (see Picard et al., 2013), and despite the different formulation of the scattering coefficient.
 404 When the grain size becomes larger ($D_o > 0.6$ mm, $SSA < 11 \text{ m}^2 \text{ kg}^{-1}$), the HUT-nlayers T_B
 405 significantly decreases, because this model empirically considers multiple scattering and is based
 406 on the 1-flux RT simplification, leading to underestimate downward-propagated T_B and then
 407 upward reflected and backscattered signal. Multiple scattering increasing with grain size tends to
 408 increase the upward radiation, compensating for the T_B attenuation.



409



410
 411 **Fig. 2** T_B variation at 37 GHz as a function of the optical diameter (D_o) of grain size for the four
 412 models. Top: T_B at the Vertical polarization; Bottom: Polarization ratio (H-pol/V-pol).
 413 Simulations performed using Eq. 11 for the snow grain size definitions and the Wegmüller and
 414 Mätzler (1999) soil model (Table 1); Soil temperature = 273 K; soil roughness = 0.19 cm,
 415 dielectric permittivity = 4.53 and the polarization reflectivity factor beta = 1.1 (Montpetit et al.,
 416 2015a); snow density = 250 kg.m⁻³; snow depth = 1 m; Snow temperature = 263 K; no stickiness
 417 and no ice lens. The incidence angle of T_B simulations is 55°.

418
 419 The main polarization effects arise from reflections at layer interfaces, and are at their maximum
 420 near the Brewster angle (around 55° at 37 GHz), leading to a significant decrease of the T_B (H-
 421 pol) with incidence angle, while T_B V-pol is weakly independent of the incidence angle. Fig. 2
 422 (bottom) shows the Polarization Ratio (PR = T_B H-pol/ T_B V-pol) variations for the four models as
 423 a function of the optical grain size simulated for a fixed incidence angle of 55°. DMRT-ML and
 424 DMRT-QMS are also identical in this case. The HUT model practically neglects the scattering
 425 polarization variations with growing grain size, while DMRT-ML/-QMS and MEMLS models
 426 show different trends in PR variations with grain size. The MEMLS volume scattering in snow is
 427 slightly sensitive to polarization (Wiesmann et al., 1998) with a weak PR increase of 2% when

428 the grain size increases between $D_0 = 0.1$ to 0.6 mm, while DMRT-ML/-QMS decreases by 4%,
429 leading to a difference of about 7% compared to MEMLS for grain sizes above 0.6 mm (Fig. 2,
430 bottom).

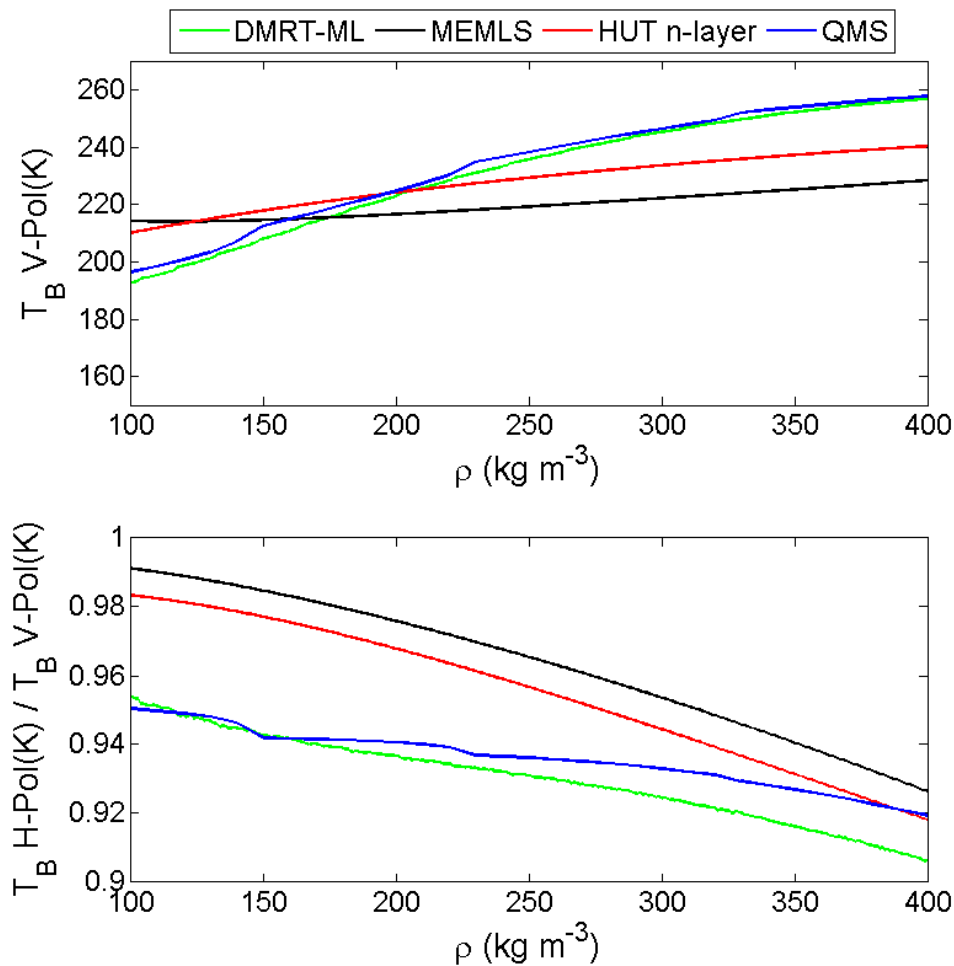
431 For a given fixed density, the polarization is modulated by 2 mechanisms: snow scattering and
432 interface reflection. As snow-air interface reflections are similarly treated in each model
433 (assuming Fresnel's reflection) and because the density remains constant in these simulations, the
434 differences between the three types of models (DMRT-ML/-QMS; HUT-nlayers and MEMLS)
435 result from the differences in the radiative transfer solution. As a matter of fact, polarization
436 effects are generated by volume scattering driven by the granular structure of the medium, i.e. by
437 a combined effect of snow grain size and density (see Mätzler, 1997) and also of stickiness for
438 DMRT-ML/-QMS (see Picard et al., 2013). The observed differences in PR variations in Fig. 2
439 (bottom) could thus likely governed by differences between the radiative transfer processing of
440 the diffuse scattering component of the signal. The results for lower incidence angles (i.e. not
441 Brewster) are similar.

442 We performed simulations (not shown) using a new model (in progress, unpublished) using the
443 same N-flux solver used in DMRT-ML but which can compute scattering coefficients with either
444 the DMRT theory (as in DMRT-ML and DMRT-QMS) or IBA (as in MEMLS). In both cases,
445 assuming the same scattering theory, the results show a decrease of the PR with increasing D_0 ,
446 while the MEMLS-IBA (6-flux) shows an increase of the PR. This suggests that the radiative
447 transfer processing, specifically 6-flux versus N-flux, could be the cause of the different
448 behaviors observed in Figure 2 (bottom), but further exploration of the role of the solver is
449 needed,

450
451 The patterns of T_B variation with snow density show similar behaviors between models but at
452 different amplitudes (Fig. 3). Here, D_0 is considered constant and equal to 0.25 mm. Over the
453 range of density variation shown, below 400 kg m^{-3} (i.e. below 44% fractional volume), at

454 vertical polarization, DMRT-ML/-QMS shows a greater sensitivity, ΔT_B V-pol of 40 K for
 455 density from 150 to 300 $\text{kg}\cdot\text{m}^{-3}$, than MEMLS and HUT which vary slightly. For low snow
 456 density between 150 and 200 $\text{kg}\cdot\text{m}^{-3}$ the four models are similar, but at a high snow density of
 457 400 $\text{kg}\cdot\text{m}^{-3}$, the T_B (V-pol) difference between DMRT-ML/-QMS and MEMLS is 28.5 K. (and
 458 21.3 K at H polarization) (Fig. 3, top). For coarser grain size (not shown), the differences in T_B
 459 V-pol versus density variations between models are amplified, due to the difference in scattering
 460 processing in each model.

461 PR variations in relation to density show parallel trends (Fig. 3, bottom), but the decrease in PR
 462 when density increases shows significant differences in slope values for each model (more than
 463 2% difference at low density for MEMLS and HUT compared to both DMRT models). For high
 464 densities (near 400 $\text{kg}\cdot\text{m}^{-3}$), this decrease is greater with DMRT-ML than DMRT-QMS.



465
 466 **Fig. 3** Same as Fig. 2, but for density ($D_0 = 0.25$ mm).

467

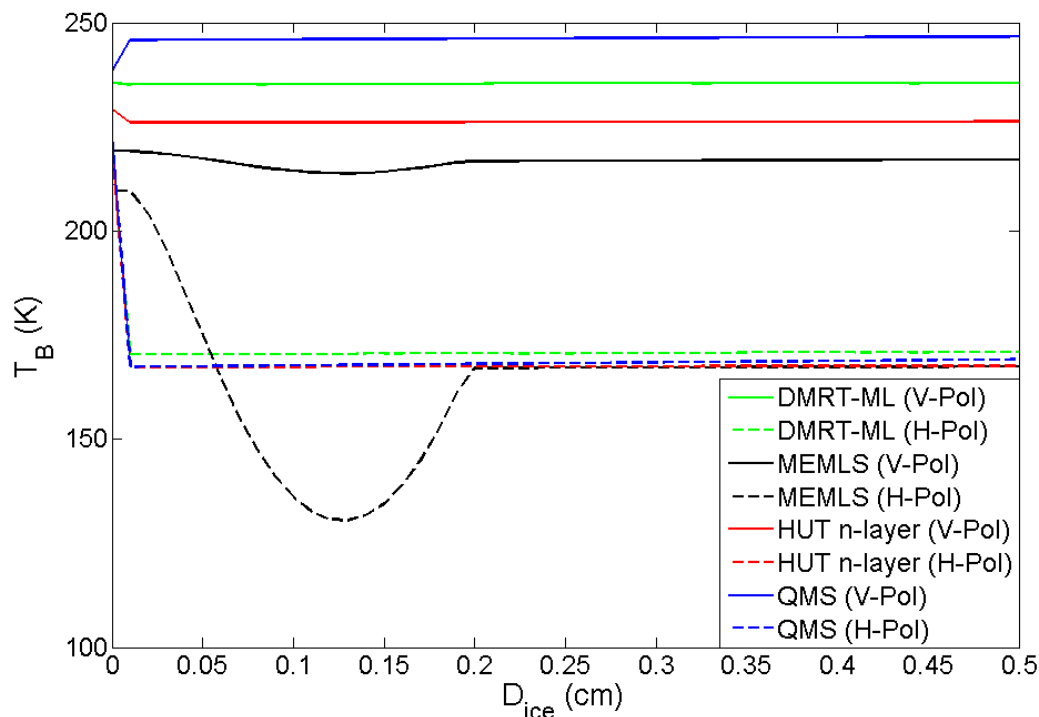
468 T_B H-pol varies as a function of density change between interface layers, mainly from reflection
469 at the snow-air interface, and of snow scattering (grain size). Since Fresnel reflection is
470 considered here, surface reflection depends on the snow dielectric constant and thus the density.
471 Assuming a constant grain size (as in Fig. 3), as density increases, the reflection coefficient
472 increases and T_B H-pol decreases, leading to the decrease in PR (as T_B V-pol is relatively
473 constant at the Brewster angle). In other words, where snowpack evolution features slow
474 metamorphism as is observed in Antarctica, PR clearly decreases with density. This was shown
475 by Picard et al. (2014) from surface-based measurements at Dome Concordia (East Antarctica).
476 Champollion et al. (2013) also showed that the observed 2000-2010 AMSR-E PR increase was in
477 agreement with the observed decreasing surface snow density, also at Dome Concordia.

478 However, when the snowpack evolves during the winter through various metamorphic processes
479 (increasing grain size), increasing layering (alternation of high- and low-density layers) and
480 increasing density processes, PR direction changes over time appear less clear. Moreover, the
481 surface roughness would produce a more diffuse scattering distribution, leading to weaker
482 polarization, while ice layers or wind-slab snow crusts lead to a significant degree of polarization
483 (e.g. Mätzler, 1982, 1994; Grenfell and Putkonen, 2008; Dolant et al., 2016). In general, since
484 surface density and state are the most important characteristics influencing polarization, one
485 expects a decrease in PR with time from snowfall. The DMRT simulations showed a PR decrease
486 for both increasing grain size and density processes in the synthetic cases considered here (Fig. 2
487 and 3), while MEMLS and HUT show a PR decrease only as a function of increasing density.

488

489 The third sensitivity analysis (Fig. 4) shows the effect of a thin ice layer put at the top of the
490 snowpack for the four models. At V-pol, there are almost no T_B variations due to ice lens while
491 TB H-pol is reduced by up to 65 K when an ice lens is introduced. The stronger decrease in H-pol
492 (ice lens vs. no ice) compared to the one at V-pol comes from the higher sensitivity to layer

493 interface reflectivity at H-pol. Note that, in Fig. 4, the differences in TB V-pol amplitudes
 494 between models result from the configuration (Do and density) used for the simulations (see Fig.
 495 2 and 3). Moreover, ice layer thickness variations have no impact on T_B variation, except when
 496 using the MEMLS model for thin ice layers. Around $D_{ice} = 0.125$ mm, MEMLS is as much as 43
 497 K lower at H-pol than the DMRT and HUT models. This significant T_B decrease simulated by
 498 MEMLS for H polarization that appears for ice thickness under $\lambda/2$ is due to the coherent
 499 reflection that dominates the microwave behavior for layers of the size $\lambda/4$ (Weismann and
 500 Mätzler, 1999). The DMRT-ML and HUT-nlayers models do not take into account this
 501 attenuation effect of the quarter-wavelength resonance. In practice, as the ice layer thickness
 502 spatially varies in the footprint of the sensor (Rutter et al., 2014), such effects are generally less
 503 pronounced than in simulations, but can be clearly observed for thin ice lenses on or in the
 504 snowpack (see Montpetit et al., 2013; Roy et al., 2016).



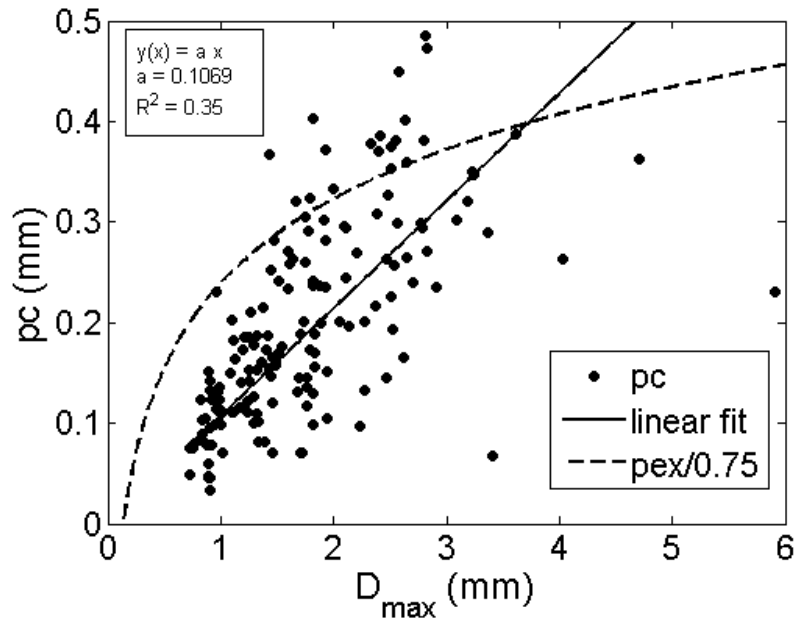
505
 506 **Fig. 4** T_B variation at 37 GHz as a function of an ice layer thickness (D_{ice}) put on the top of the
 507 snowpack for the four models (full lines: V-pol; dotted lines: H-pol). Snowpack and soil
 508 properties are the same as in Fig. 2 and 3 ($D_o = 0.25$ mm and density = 250 kg.m^{-3}). Ice lens

509 density = 917 kg m^{-3} and ice lens temperature is the same as snow temperature.

510

511 *4.2 Snow grain database comparison analysis*

512 | We analyzed 159 photographed plates from the 32 studied snowpits, corresponding to a total of
513 | 36,384 digitized grains with an average of 229 grains per plate. For each plate, we considered the
514 | mean maximum dimension of all the grains on the plate (D_{max}). For each corresponding layer, we
515 | also measured the snow SSA and density. It is well known that the relationship between D_0 and
516 | D_{max} is not one-to-one (see Langlois et al., 2010; Leppänen et al., 2015). However, in order to
517 | evaluate the consistency of the datasets, Fig. 5 shows the relationship between the calculated
518 | correlation length derived from SSA and density measurements (Eq. 5, $\phi = 1$) and the
519 | corresponding mean D_{max} for all the samples. The results show that this relationship appears
520 | somewhat scattered as expected, and more linear rather than the logarithmic relationship
521 | suggested by Mätzler (2002). But note that, for the latter case (for 20 samples), D_{max} values were
522 | visually determined, whereas, in our case, D_{max} were derived from digitized contours. The
523 | digitization, the very large number of data and also the computation of the mean values (over
524 | hundreds of grains) could explain that our D_{max} values are different than those visually
525 | determined. The digitization of grain size is considered as a more reproducible and more precise
526 | approach. We also considered (not shown) median values instead of arithmetic means that did not
527 | give significant differences. On the other hand, the correlation lengths in the Mätzler (2002)
528 | database were measured (micro-CT) whereas we derived this parameter from SSA and density
529 | measurements. The reason for the differences between these micro-structure metrics (D_{max} , SSA,
530 | correlation length), discussed for example by Löwe and Picard (2015), and which may also result
531 | from differences in snow types (alpine, boreal, arctic), is beyond the scope of this paper. This
532 | unique database (coincident values of D_0 , ρ_c and D_{max}) was used to provide specific inputs to
533 | drive each model considered in order to simulate the brightness temperatures.



534

535 **Fig. 5** Relationship between the correlation length derived from SSA and density measurements
 536 (p_c , calculated with Eq. 5, $\phi = 1$) and the mean maximum geometrical extent of the grains (D_{\max})
 537 measured by digitized photographs of snow grains (each point of this graph corresponds in
 538 average to 229 digitized grains per sample). The dotted curve corresponds to the logarithmic
 539 relationship observed by Mätzler (2002).

540

541 **4.3 Model comparison using measured inputs**

542 As DMRT-QMS is very similar to DMRT-ML, only three models are considered in the
 543 following: DMRT-ML, HUT-nlayers and MEMLS. For all the sites described in the Table 4, Fig.
 544 6 compares the 3 model simulations against surface-based measured brightness temperatures with
 545 exactly the same soil parameters (Table 3), and for the snow microstructure metrics derived either
 546 from SSA or D_{\max} measurements. DMRT-ML (Fig. 6a), HUT_Do (Fig. 6b) and MEMLS_Do
 547 (Fig. 6c) were driven by the scaled optical diameter of snow grain derived from SSA
 548 measurements. The HUT_ D_{\max} simulations (Fig. 6d) were driven by D_{\max} measurements using an
 549 optimized scaling factor (see Section 2). Using D_{\max} measurements, two inputs were also
 550 considered for MEMLS simulations: 1) MEMLS_ D_{\max} _pex (Fig. 6e) based on the Mätzler
 551 relationship (Durand et al., 2008, Eq. 7, see Fig. 5); and 2) MEMLS_ D_{\max} _lin (Fig. 6f) based on

552 the correlation length estimated by the observed linear relationship shown in Fig. 5. These model
 553 inputs are summarized in Table 5.

554

555 The root mean square errors (RMSE) and the biases are compared in Table 6 and shown in Fig. 7
 556 for the three frequencies (11, 19 and 37 GHz) and each polarization. Note that the full set of input
 557 snow properties and 11 GHz radiometer measurements are only available for two sites, hence, the
 558 analysis focuses on 19 and 37 GHz.

559

560

561 **Table 5** Summary of the inputs used for the model simulations. The corresponding equations
 562 (Eq.) are explained in Section 2.

Model configuration	Grain size measurements	Input parameters	Eq.	Fig.
DMRT-ML	SSA	$D'o = 6 \cdot 10^3 \cdot 3.3 / (\rho_{ice} \cdot SSA)$	2	6a
MEMLS_Do	SSA	$p'_c = 4 \cdot 10^3 \cdot 1.3(1 - \nu) / (\rho_{ice} \cdot SSA)$	6	6c
MEMLS_D _{max} p _{ex}	D _{max}	- $p_{ex} = 0.18 + 0.09 \ln(D_{max})$ for $\nu > 0.2$ and $D_{max} > 0.125$ mm - $p_{ex} = 0.05 \pm 0.017$ otherwise	7	6e
MEMLS_D _{max} lin	D _{max}	$p_c = 0.1069 D_{max}$	Fig. 5	6f
HUT_Do	SSA	$Do_{eff} = 6 \cdot 10^3 \cdot 3.7 / (\rho_{ice} \cdot SSA)$	9	6b
HUT_D _{max}	D _{max}	$D_{max,eff} = 0.5 D_{max}$	-	6d

563

564

565

566

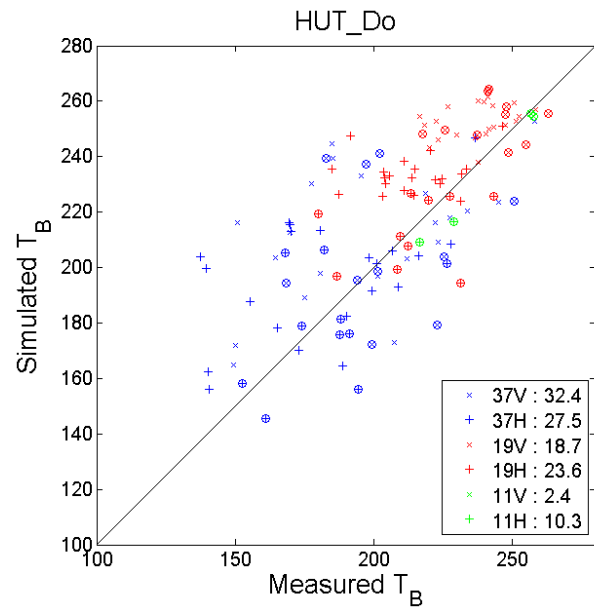
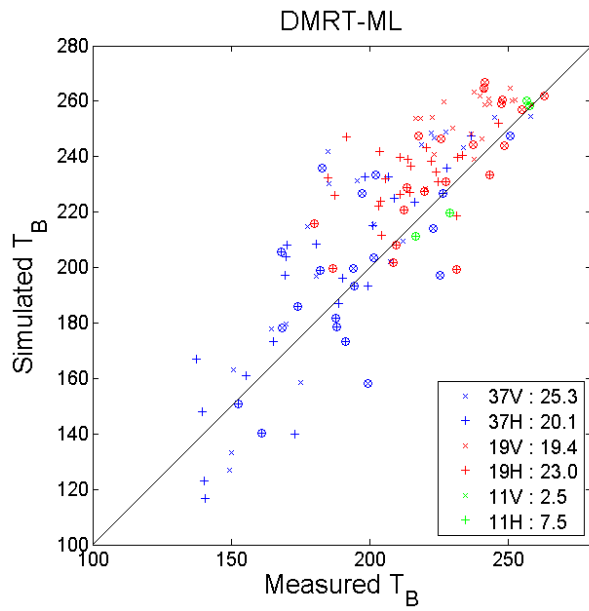
567

568 **Table 6** Bias (B) and RMSE (R) (K) between simulated and measured T_{BS} for each frequency
 569 and polarization and for each model driven by specific inputs (described in Table 5). Bold:
 570 minimum bias and RMSE values of each line respectively (but not necessarily statistically
 571 significant).

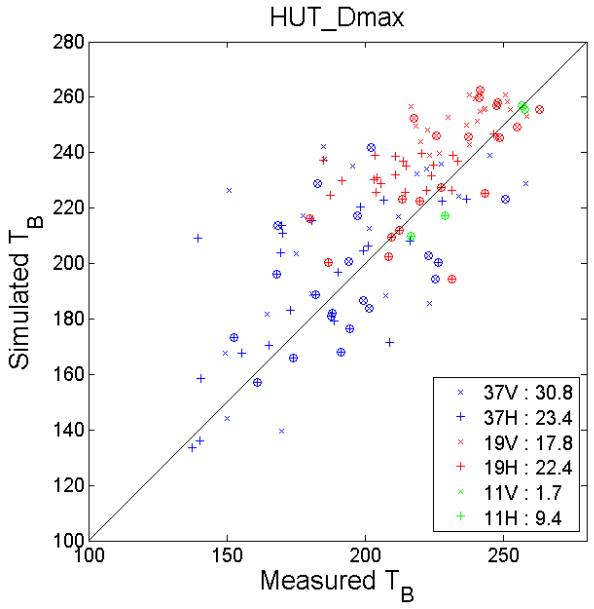
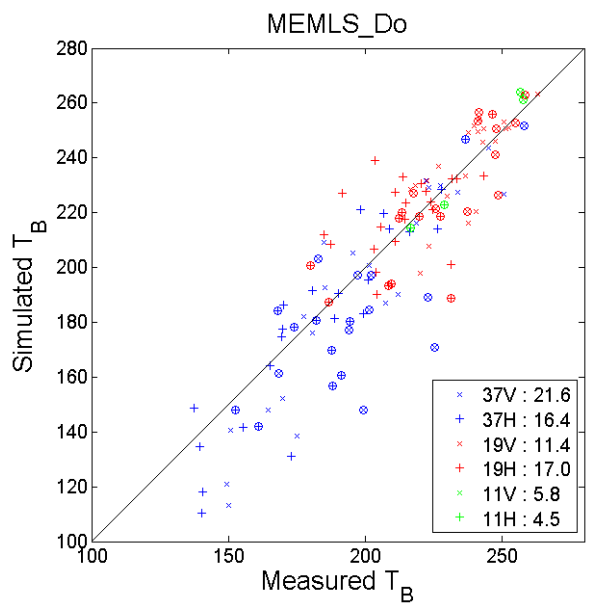
Model	DMRT-ML		MEMLS						HUT			
	Do $\phi=3.3$		Do $\phi=1.3$		D _{max_lin} (Fig. 5)		D _{max_pex} Eq.7		Do $\phi=3.7$		D _{max} $\phi=0.5$	
Inputs	B	R	B	R	B	R	B	R	B	R	B	R
11V	2.1	2.5	5.5	5.8	5.5	5.5	7.8	7.8	-2.1	2.4	-1.1	1.7
11H	-7.3	7.5	-4.1	4.5	-3.9	4.9	-2.6	4.1	-10.0	10.3	-9.1	9.4
19V	16.0	19.4	0.1	11.4	6.2	14.5	15.0	18.2	13.8	18.7	13.6	17.8
19H	14.7	23.0	2.9	17.0	7.8	18.8	15.0	23.7	8.5	27.5	13.4	22.4
37V	11.0	25.3	-10.8	21.6	-10.8	26.7	-10.8	24.4	11.3	32.4	9.6	30.8
37H	7.5	20.1	-4.9	16.4	-3.3	19.9	9.0	21.4	8.5	27.5	6.7	23.4
All	7.3	16.3	-3.1	12.8	0.3	15.0	5.6	16.6	5.9	19.1	5.5	17.6

572
 573
 574 For the 32 analyzed snowpits, the overall results at 19 and 37 GHz for the 6 model configurations
 575 show mean bias values of the order of 6 K, ranging from -10.8 to 16 K depending on the model,
 576 configuration and frequency considered. The mean RMSE value is of the order of 20 K (19 GHz)
 577 and 24 K (37 GHz), ranging from 11.4 to 32.4 K. Large differences in bias appear between
 578 models (MEMLS with negative biases), and no significant differences in bias or RMSE can be
 579 seen between polarizations. Note that except for HUT_Dmax ($0.5 \cdot D_{max}$), the models were not
 580 specifically optimized for the new cases considered in this study, since the used scaling factors
 581 were derived from previous publications over different sites.

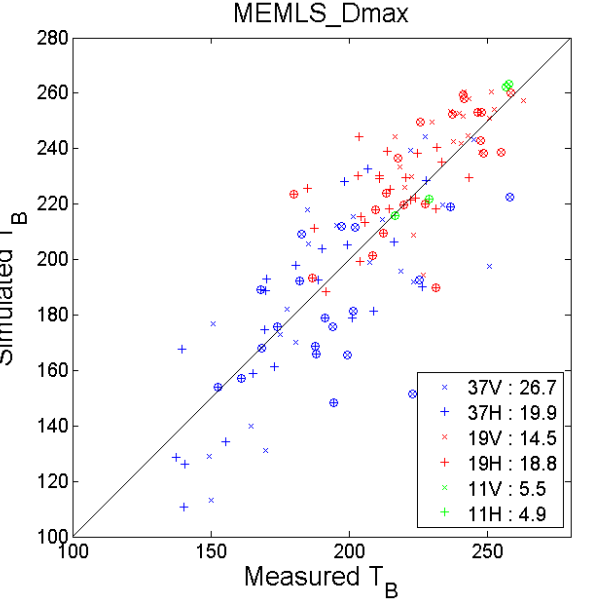
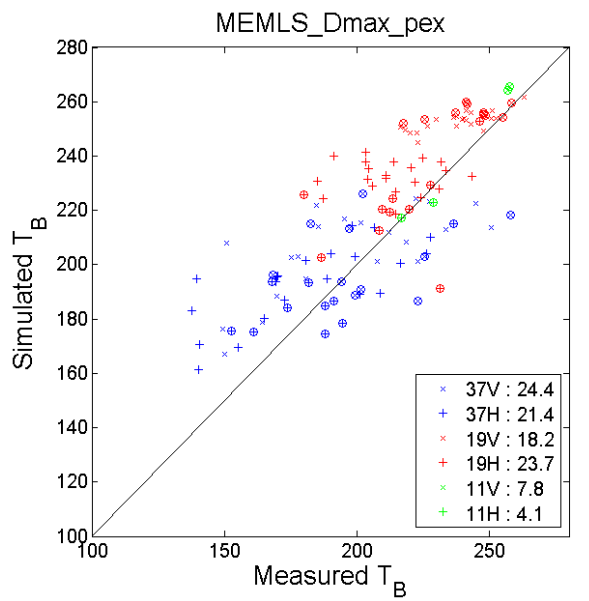
582
 583



584

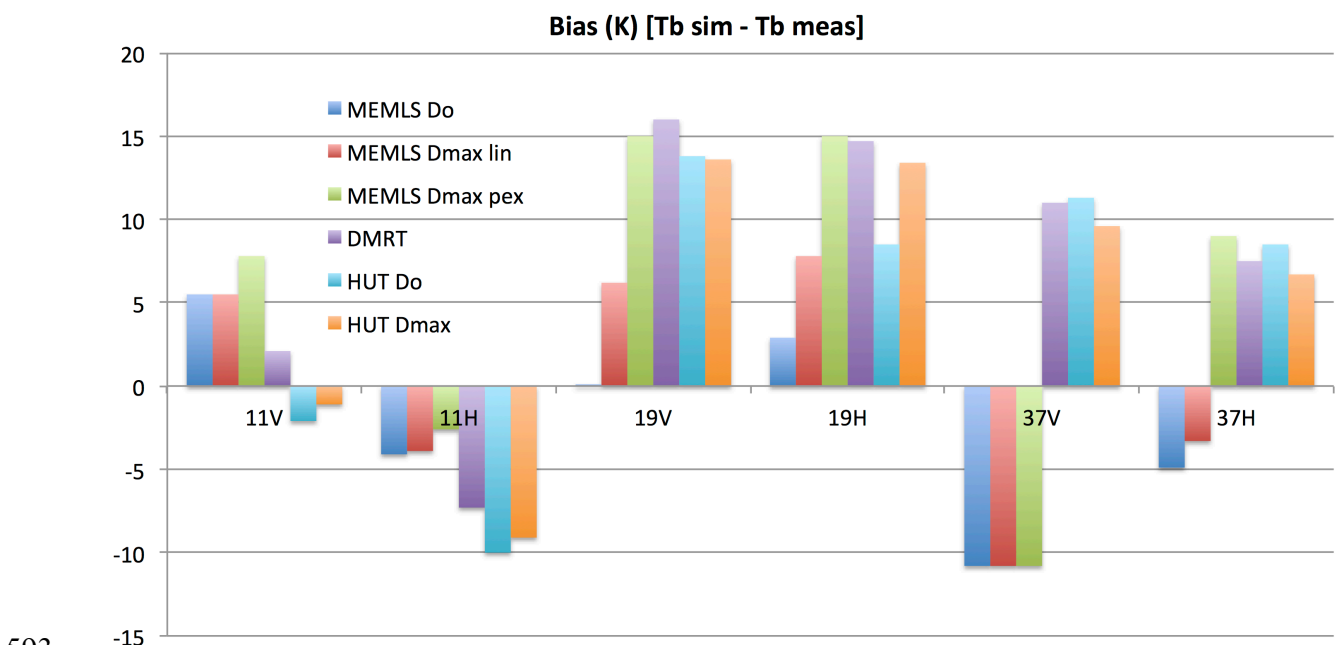
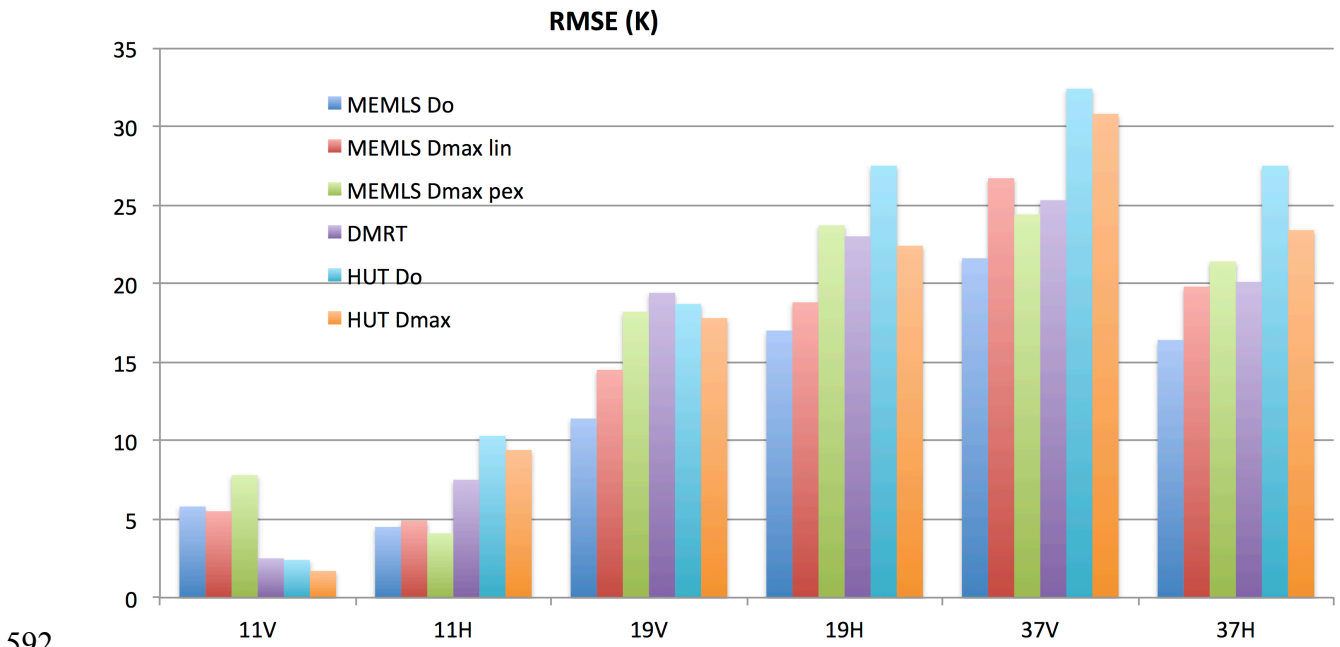


585



586

587 **Fig. 6** Scatterplot comparing simulated brightness temperatures against measurements for each
 588 frequency and polarization for all the sites (described in Table 4). Circled symbols represent sites
 589 that included ice lenses. a: DMRT, b: HUT_Do (right); c: MEMLS_Do; d: HUT_Dmax; e:
 590 MEMLS_Dmax_p_{ex}; f: MEMLS_Dmax_lin. Input parameters are listed in Table 5. Values given
 591 in the figures correspond to the RMSE in Kelvin (reported in Table 6).



595 **Fig. 7** Comparison between the RMSE and biases for the 6 model configurations. The
596 corresponding values are given in Table 6.

597

598 MEMLS_Do seems to give slightly better results (mean RMSE of 14 K and 19 K, respectively at
599 19 and 37 GHz, for both polarizations) relative to other configurations and models (Fig. 6, 7 and
600 Table 6). DMRT-ML results show a mean RMSE of 21 K (19 GHz) and 23 K (37 GHz) in this
601 study, although we obtained better results for 45 other Arctic and Subarctic snowpits with the
602 same parameterization (mean RMSE of 10 K (19 GHz) and 12 K (at 37 GHz), see Roy et al.,
603 2016). The HUT model shows a lesser agreement at 37 GHz (mean RMSE of 30 K and 27 K
604 respectively for the Do and D_{\max} configuration).

605

606 MEMLS tends to underestimate the T_B at 37 GHz V-pol (negative bias), while the other models
607 tend to overestimate the simulated T_B (positive bias). This is in accordance with the comparison
608 using synthetic snowpacks (see Fig. 2, top), showing lower MEMLS T_B compared to DMRT and
609 HUT for a large range of grain sizes.

610

611 Among the three analyzed MEMLS versions, it appears that MEMLS_Do performs best,
612 compared to the D_{\max} -based simulations (an average RMSE at 19 and 37 GHz of 16.6 K, 20 K
613 and 22 K for respectively the MEMLS_Do, $_D_{\max_lin}$ and $_D_{\max_pex}$ configurations). As
614 expected, the HUT model provides a slightly lower RMSE when using D_{\max} (23.6 K) compared
615 to HUT_Do (26.5 K). Moreover, at 37 GHz, DMRT using SSA appears better than the HUT
616 model based on D_{\max} . This confirms that the scaled SSA parameter is, in general, clearly better
617 than the D_{\max} parameter for describing snow grain size for microwave radiometry no matter the
618 MEMLS or DMRT-ML model.

619

620

621 We showed (Fig. 4) that, for the synthetic snowpack, ice lens thickness within the snowpack
622 could lead to significant differences in T_B among the models. Here, we accounted for the ice layer
623 effects when they were observed in the snowpack, and the comparison shown in Fig. 6 does not
624 exhibit systematic differences between snowpits with ice layers (10 sites/32, see Table 4) and
625 those without ice layers. This first shows that ice layers can be adequately corrected for when
626 their presence and particularly their position within the snowpit is known (see Montpetit et al.,
627 2013; Roy et al, 2016), and secondly that ice layers cannot explain the differences in RMSE
628 between models.

629
630 In terms of linear regression between simulated and measured T_B (coefficient of determination R^2
631 and slope of the regression), the model comparison (Table 7) also highlights the differences
632 between models and configurations. Best results are obtained with DMRT-ML and MEMLS_Do,
633 with a mean R^2 of the order of 0.75 – 0.79 for the 4 channels (T_B at 19 and 37 GHz and both
634 polarizations). Results for these models are better at 37 GHz and with a slope slightly greater
635 than 1, meaning that the models underestimate low T_B values at this frequency ($T_B < \sim 170$ K).
636 Even if MEMLS_Dmax_lin is really better than MEMLS_Dmax_pex for both R^2 and slope
637 parameters, MEMLS_Dmax_lin performs less well than MEMLS based on Do. The HUT model
638 gives here the worst agreement against measurements. Note that, in all cases (Table 7), the T_B H-
639 pol values at 19 GHz show the lowest correlations, likely due to non-optimized processing of
640 stratification between the snow layer interfaces, assumed specular, and for the soil-snow interface
641 (roughness, for example). The statistics at 11 GHz are not included because there are only 2
642 measurements, but are included in the overall linear regression.

643

644

645

646

647 **Table 7** Comparison of linear regression parameters (coefficient of determination R^2 and slope of
 648 the regression) for simulated and measured T_B for the models shown in Fig. 6. All*: including 11
 649 GHz at H-pol and V- pol.

Model	DMRT-ML		MEMLS						HUT			
Inputs	Do $\phi=3.3$		Do $\phi=1.3$		D _{max_lin} (Fig. 5)		D _{max} p _{ex} Eq.7		Do $\phi=3.7$		D _{max} $\phi=0.5$	
	R ²	Slope	R ²	Slope	R ²	Slope	R ²	Slope	R ²	Slope	R ²	Slope
19V	0.30	0.53	0.52	0.95	0.29	0.64	0.46	0.20	0.14	0.24	0.11	0.19
19H	0.13	0.33	0.23	0.47	0.17	0.39	0.03	0.12	0.05	0.18	0.05	0.17
37V	0.63	1.07	0.72	1.04	0.45	0.78	0.31	0.29	0.13	0.34	0.19	0.43
37H	0.73	1.19	0.78	1.10	0.58	0.88	0.48	0.36	0.22	0.45	0.34	0.58
All*	0.75	1.10	0.79	1.06	0.69	0.98	0.63	0.70	0.51	0.73	0.55	0.76

650

651 At least, we compared the simulated Polar Ratio (PR H/V) at 37 GHz to the measured PR. The
 652 results show similar performance between the models (mean RMSE of 0.055). Also, we cannot
 653 conclude about the effect of the grain size on the PR trend (as simulated in Fig. 2). This relates to
 654 the fact that the sites integrate a large range of density and Do values, while Fig. 2 assumes a
 655 constant density when Do varies.

656

657 5. Discussion and conclusion

658 Over a large set of Arctic, Subarctic and boreal snow datasets, we derived a unique
 659 comprehensive snow grain size metrics database. These metrics were defined, on the one hand,
 660 by their specific surface area (SSA, from IR reflectometry measurements), and, on the other
 661 hand, for the same snow samples, by their mean maximum geometrical extent, called D_{max} ,
 662 obtained from digitized macrophotos of snow samples at each layer. Here, we did not estimate
 663 D_{max} size by visual inspection as is generally done, because of the subjectivity of that approach.
 664 The digitization of each snow grain distributed on a photographed plate is thought to be a more
 665 robust and objective approach. This dataset allowed us to compare ground-based measurements
 666 of brightness temperatures (T_B) to the simulated T_B using four models driven by their specific

667 metrics: DMRT-ML and -QMS with the optical diameter (D_o) derived from SSA measurements;
668 the HUT model with D_{max} ; and the MEMLS model driven by the correlation length which can be
669 estimated using both parameters (D_o and D_{max}). We also tested the HUT model with D_o , and we
670 compared MEMLS simulations based on 2 different relationships for correlation length
671 estimation. A total of six model configurations (Table 5) were thus analyzed (Fig. 6, 7 and Table
672 6).

673

674 Whatever the model considered, the scatterplots between simulated and measured T_B show
675 somewhat large scatters (Fig. 6) due to the inherent uncertainties on all the parameters that affect
676 the emitted signal, i.e. soil (temperature, dielectric permittivity and roughness), snow density
677 stratification, snow temperature profile and snow grain size stratification (Roy et al., 2016;
678 Durand et al., 2008). The obtained root mean square error between simulated and measured T_B
679 are in the same range of values shown in previous studies that considered the same models (Roy
680 et al., 2016; Pan et al., 2016; Löwe and Picard, 2015; Roy et al. 2013; Lemmetyinen et al.,
681 2010b). The results analyzed here are thus representative of errors commonly obtained for Arctic
682 and Subarctic snows with these models. But this is the first time that these models were
683 compared with their specific snow microstructure input data for which they were defined. These
684 results confirm first that each metric, D_o as well as pc and D_{max} , must be scaled in order to
685 minimize the RMSE between simulated and measured T_B . This aspect was discussed and partly
686 explained in previous papers (Löwe and Picard, 2015; Roy et al. 2013; Kontu and Pulliainen,
687 2010). Secondly, the results show that the snow microstructure metric based on D_o appears to
688 give better results than the metric defined by D_{max} (Table 6). This may be due to the fact that
689 microwave scattering is more directly related to D_o than to D_{max} . Also, even if the shadow box
690 used to measure D_{max} , is more accurate than visual estimates, the D_o value, derived from snow
691 SSA measurements, could give a better estimate of the effective mean size over the grain size
692 distribution per layer than the mean value of D_{max} measurements.

693
694 It is difficult to conclude on the performance of DMRT-ML, HUT and MEMLS due to the large
695 observed scatter on simulations, although the MEMLS model appears here slightly better for the
696 snowpits analyzed in this study. We found a mean RMSE at high frequencies (19 and 37 GHz) of
697 16.6 K, 22.0 K and 23 K respectively for MEMLS_Do, DMRT-ML and HUT_D_{max}. However, as
698 mentioned above, a specific optimization could have been made on the input parameters for each
699 model (on the ϕ scaling factors) that would have a different effect on the models and change the
700 results comparison. This scaling factor may also depend on the types of snow, i.e. on
701 metamorphism processes and shape (see Löwe and Picard, 2015; Krol and Löwe, 2016).
702 However, the comparison shown here between the four models using a synthetic snowpack (Fig.
703 2, 3 and 4) clearly shows the intrinsic difference in radiative transfer behavior as a function of
704 grain size, density and ice lens variations within the snowpack, in particular for the polarization
705 ratio (T_B H-pol / T_B V-pol).

706
707 In conclusion, to date, from a practical point of view using in-situ measurements of snow
708 properties, this paper shows that the SSA parameter appears to be the most relevant parameter for
709 characterizing snow microstructure, even if it must be scaled to be used for microwave
710 simulations. Snow tomography could give more precise microstructure characterization but
711 requires significant processing time. When suitably scaled for each model (MEMLS and DMRT-
712 ML), the SSA parameter produces the same order of error magnitude in simulated brightness
713 temperature. From a physical perspective, Löwe and Picard (2015) showed that MEMLS and
714 DMRT-ML are in fact very similar.

715 716 **Acknowledgements**

717 This study was supported by the National Sciences and Engineering Research Council of Canada
718 (NSERC), the Canadian Foundation for Innovation, Environment Canada, NASA-Goddard (L.B.)

719 and by the Programme de développement de partenariats stratégiques en matière d'enseignement
720 et de recherche of the Conseil franco-québécois de la coopération universitaire, a France-Québec
721 research collaboration. The authors would like to thank Patrick Cliche and Miroslav Chum for
722 creating the Shadow-box, all participants to the field works for their contributions to obtain the
723 ground-based measurements, and Peter Toose and Chris Derksen (Environment Canada) for
724 providing part of the Churchill data.

725

726 **References**

727 Armstrong, R., & Brodzik, M. (2002). Hemispheric-scale comparison and evaluation of passive-
728 microwave snow algorithms. *Annals of Glaciology*, 34, 38–44.

729 Asmus K.W. and C. Grant (1999). “Surface based radiometer (SBR) data acquisition system,”
730 *Int. J. Remote Sens.*, 20(15/16), 3125–3129.

731 Brucker, L., Picard, G., Arnaud, L., Barnola, J.M., Schneebeli, M., Brunjail, H., Lefebvre, E. and
732 Fily, M. (2011), Modeling time series of microwave brightness temperature at Dome C,
733 Antarctica, using vertically resolved snow temperature and microstructure measurements. *J. of*
734 *Glaciology*, 57(201), 171-182.

735 Champollion, N., Picard, G., Arnaud, L., Lefebvre, E., and Fily, M.: Hoar crystal development
736 and disappearance at Dome C, Antarctica: observation by near-infrared photography and
737 passive microwave satellite, *The Cryosphere*, 7, 1247-1262, doi:10.5194/tc-7-1247-2013.

738 Chang W., S. Tan, J. Lemmetyinen, L. Tsang, X. Xu, X. Li and S. Yueh (2014). Dense Media
739 Radiative Transfer Applied To SnowScat and SnowSAR, *IEEE Journal of Selected Topics in*
740 *Applied Earth Observations and Remote Sensing*, 7(9), 3811 – 3825.

741 Colbeck S., E. Akitaya, R. Armstrong, H. Gubler, J. Lafeuille, K. Lied, D. McClung, and E.
742 Morris (1990), *The International Classification for Seasonal Snow on the Ground*.
743 Wallingford, U.K.: Int. Commission Snow Ice Int. Assoc. Sci. Hydrol., Working Group Snow
744 Classification.

745 [Courtemanche B., B. Montpetit, A. Royer and A. Roy \(2015\). Creation of a lambertian](#)
746 [microwave surface for retrieving the downwelling contribution in ground-based radiometric](#)
747 [measurements. *IEEE Geoscience and Remote Sensing Letters*, 12\(3\), 462-466.](#)

748 Dolant C., A. Langlois, B. Montpetit, L. Brucker, A. Roy and A. Royer (2016). Development of
749 a rain-on-snow detection algorithm using passive microwave radiometry. *Hydrol.*
750 *Process.*, Published online in Wiley Online Library, DOI: 10.1002/hyp.10828

751 Domine, F., Albert, M. , Huthwelker, T. , Jacobi, H. W. , Kokhanovsky, A. A. , Lehning, M. ,
752 Picard, G. and Simpson, W. R. (2008): Snow physics as relevant to snow photochemistry ,
753 *Atmospheric Chemistry and Physics*, 8 , 171-208.

754 Dupont, F., Picard, G., Royer, A., Fily, M., Roy, A., Langlois, A., and Champollion, N. (2014).
755 Modeling the Microwave Emission of Bubbly Ice: Applications to Blue Ice and Superimposed
756 Ice in the Antarctic and Arctic, *IEEE T. Geosci. Remote*, 52, 6639–6651,
757 doi:10.1109/TGRS.2014.2299829.

758 Durand, M., E. J. Kim, and S. A. Margulis (2008), Quantifying uncertainty in modeling snow
759 microwave radiance for a mountain snowpack at the point-scale, including stratigraphic
760 effects, *IEEE Trans. Geosci. Remote Sens.*, 46, 1753–1767.

761 Fierz, C., Armstrong, R. L., Durand, Y., Etchevers, P., Greene, E., McClung, D. M., Nishimura,
762 K., Satyawali, P. K., and Sokratov, S. (2009). *The International Classification for Seasonal*
763 *Snow on the Ground*, IHP-VII Technical Documents in Hydrology, 83, IACS Contribution (1),
764 UNESCO-IHP, Paris.

765 Gallet, J.-C., Domine, F., Zender, C. S., and Picard, G. (2009). Measurement of the specific
766 surface area of snow using infrared reflectance in an integrating sphere at 1310 and 1550 nm,
767 *The Cryosphere*, 3, 167–182, doi:10.5194/tc-3-167-2009.

768 Grenfell T.C. and Putkonen J. (2008). A method for the detection of the severe rain- on-snow
769 event on Banks Island, using passive microwave remote sensing. *Water Resources Research*
770 44:W03425: DOI:10.1029/2007WR005929.

771 Grody, N. (2008). Relationship between snow parameters and microwave satellite measurements:
772 Theory compared with Advanced Microwave Sounding Unit observations from 23 to 150
773 GHz, *J. Geophys. Res.*, 113, 17 pp., doi:10.1029/2007JD009685.

774 Hallikainen M.T., F. T. Ulaby, and T. E. Van Deventer (1987). “Extinction behavior of dry snow
775 in the 18-to 90-GHz range,” *IEEE Trans. on Geoscience and Remote Sensing*, 6, 737–745.

776 Huang S. and L. Tsang (2012). Electromagnetic Scattering of Randomly Rough Soil Surfaces
777 Based on Numerical Solutions of Maxwell Equations in Three-
778 Dimensional Simulations Using a Hybrid UV/PBTG/SMCG Method, *IEEE Trans. on*
779 *Geoscience and Remote Sensing*, 50(10), 4025-4035.

780 Jin, Y. Q. (1994). *Electromagnetic scattering modelling for quantitative remote sensing*, World
781 Scientific, Singapore, 1994.

782 Kelly, R., Chang, A., Tsang, L., & Foster, J. (2003). A prototype AMSR-E global snow area and
783 snow depth algorithm. *IEEE Trans. on Geoscience and Remote Sensing*, 41(2), 230–242.

784 Kontu, A. and J. Pulliainen (2010). Simulation of spaceborne microwave radiometer mea-
785 surements of snow cover using in situ data and brightness temperature modeling. *IEEE*
786 *Transactions on Geoscience and Remote Sensing*, 48(3), 1031–1044.

787 [Krol Q. and H. Löwe \(2016\). Relating optical and microwave grain metrics of snow: The](#)
788 [relevance of grain shape. *The Cryosphere Discuss.*, doi:10.5194/tc-2016-119.](#)

789 Langlois A. (2015). *Applications of the PR Series Radiometers for Cryospheric and Soil*
790 *Moisture*. Research, Technical Report, © Radiometrics Corporation, 2015, 40p.

791 Langlois, A., A. Royer, B. Montpetit, G. Picard, L. Brucker, L. Arnaud, P. Harvey-Collard, M.
792 Fily and K. Goïta (2010). On the relationship between snow grain morphology and in-situ near
793 infrared calibrated reflectance photographs. *Cold Regions Science and Tech.*, 61(1), 34-42.

794 Lemmetyinen J., A. Kontu, A. Rees, C. Derksen, and J. T. Pulliainen (2010b). Comparison of
795 multiple layer snow emission models,” presented at the *2010 11th Specialist Meeting on*
796 *Microwave Radiometry and Remote Sensing of the Environment (MicroRad)*, Washington,

797 DC, 2010, pp. 99–103.

798 Lemmetyinen J., C. Derksen, P. Toose, M. Proksch, J. Pulliainen, A. Kontu, K. Rautiainen, J.
799 Seppänen, M. Hallikainen (2015). Simulating seasonally and spatially varying snow cover
800 brightness temperature using HUT snow emission model and retrieval of a microwave
801 effective grain size. *Remote Sensing of Environment* 156, 71–95.

802 Lemmetyinen, J., Pulliainen, J., Rees, A., Kontu, A., Qiu, Y., & Derksen, C. (2010a). Multiple
803 layer adaptation of the HUT snow emission model: comparison with experimental data. *IEEE*
804 *Transactions on Geoscience and Remote Sensing*, 48, 2781–2794.

805 Leppänen, L., A. Kontu, J. Vehviläinen, J. Lemmetyinen, and J. Pulliainen (2015). Comparison
806 of traditional and optical grain size field measurements with SNOWPACK simulations in a
807 taiga snowpack. *J. Glaciol.*, 61(225), 151-162.

808 Lesaffre B., E. Pougatch et E. Martin (1997). Détermination objective des caractéristiques des
809 grains de neige à partir d'images. *La Houille Blanche*, 7, 76-82, DOI: 10.1051/lhb/1997068.

810 Liang D., X. Xu, L. Tsang, K. M. Andreadis and E. G. Josberger (2008). The effects of layers in
811 dry snow on its passive microwave emissions using dense media radiative transfer theory
812 based on the quasicrystalline approximation (QCA/DMRT), *IEEE Trans. Geos. Rem. Sens.*,
813 46(11), 3663-3671.

814 Liebe, H. (1989). MPM: An atmospheric millimeter-wave propagation model. *Int. J. of Infrared*
815 *and Millimeter Waves*, 10(6), 631–650.

816 Löwe, H. and Picard, G. (2015). Microwave scattering coefficient of snow in MEMLS and
817 DMRT-ML revisited: the relevance of sticky hard spheres and tomography-based estimates of
818 stickiness, *The Cryosphere*, 9, 2101-2117.

819 Löwe, H., Riche, F., and Schneebeli, M. (2013), A general treatment of snow microstructure
820 exemplified by an improved relation for thermal conductivity, *The Cryosphere*, 7, 1473–1480.

821 Mätzler C. and A. Wiesmann (2014). *Microwave Emission Model of Layered*
822 *Snowpacks; Documentation for MEMLS, Version 3*. Institute of Applied Physics - University

823 of Bern Sidlerstrasse 5, 3012 Bern, Switzerland, 26 pp.

824 Mätzler C. (Ed.), P.W. Rosenkranz, A. Battaglia and J.P. Wigneron (Co-Eds.) (2006). Thermal
825 Microwave Radiation - Applications for Remote Sensing, *IET Electromagnetic Waves Series*
826 52, London, UK.

827 Mätzler C. (1996, 2004). "Notes on microwave radiation from snow samples and from a layered
828 snowpack", IAP Research Report 96-9, University of Bern, Switzerland, (1996).

829 Mätzler, C. (2002), Relation between grain-size and correlation length of snow, *J. Glaciol.*, 48,
830 461–466.

831 Mätzler C. and A. Wiesmann (1999). "Extension of the Microwave Emission Model of Layered
832 Snowpacks to Coarse-Grained Snow", *Remote Sensing of Environment*, 70(3), 317-325.

833 Mätzler C. (1998). Improved Born Approximation for scattering of radiation in a granular
834 medium, *J. Appl. Phys.*, 83(11), 6111-6117.

835 Mätzler, C. (1994). Passive microwave signatures of landscapes in winter. *Meteorology*
836 *Atmospheric Physics*, 54, 241–260.

837 Mätzler, C. (1997). "Autocorrelation functions of granular media with free arrangement of
838 spheres, spherical shells or ellipsoids", *J. Applied Physics*, 81(3), 1509-1517.

839 Mesinger, F., Dimego, G., Kalnay, E., Mitchell, K., Shafran, P. C., Ebisuzaki, W., et al. (2006).
840 North American regional reanalysis. *Bull. of the American Meteorol. Soc.*, 87(3), 343–360.

841 Montpetit B., A. Royer, J.-P. Wigneron, A. Chanzy and A. Mialon (2015a). Evaluation of multi-
842 frequency bare soil microwave reflectivity models. *Remote Sensing of Enviro.*, 162, 186 - 195.

843 Montpetit B., A. Royer, A. Roy and A. Langlois (2015b). In-situ passive microwave
844 parameterization of sub-arctic frozen organic soils. *IEEE Geoscience and Remote Sensing*
845 *Letters*, Submitted.

846 Montpetit B., Royer A., Langlois A., Cliche P., Roy A., Champollion N., Picard G., Domine F.,
847 Obbard R. (2012). New short wave infrared albedo measurements for snow specific surface
848 area retrieval, *Journal of Glaciology*, 58(211), doi: 10.3189/2012JoG11j248.

849 Montpetit, B., Royer, A., Roy, A., Langlois, A. and Derksen, C. (2013). Snow microwave
850 emission modeling of ice lenses within a snowpack using the Microwave Emission Model for
851 Layered Snowpacks, *IEEE Trans. on Geoscience and Remote Sensing*, 51(9), 4705- 4717.

852 Pan J., Durand M., Sandells M., Lemmetyinen J., Kim E.J., Pulliainen J., Kontu A. and C.
853 Derksen (2016). "Differences Between the HUT Snow Emission Model and MEMLS and
854 Their Effects on Brightness Temperature Simulation," *IEEE Transactions on Geoscience and*
855 *Remote Sensing*, 54(4), 2001-2019, doi: 10.1109/TGRS.2015.2493505

856 Picard, G., Brucker, L., Roy, A., Dupont, F., Fily, M., Royer, A., and Harlow, C. (2013).
857 Simulation of the microwave emission of multi-layered snowpacks using the Dense Media
858 Radiative transfer theory: the DMRT-MLmodel, *Geosci. Model Dev.*, 6, 1061–1078,
859 doi:10.5194/gmd-6-1061-2013.

860 Picard, G., Royer, A., Arnaud, L., and Fily, M. (2014). Influence of meter-scale wind-formed
861 features on the variability of the microwave brightness temperature around Dome C in
862 Antarctica, *The Cryosphere*, 8, 1105–1119, doi:10.5194/tc-8-1105-2014.

863 Proksch M., C. Mätzler, A. Wiesmann, J. Lemmetyinen, M. Schwank, H. Löwe and
864 M. Schneeball (2016). MEMLS3&a: Microwave Emission Model of Layered Snowpacks
865 adapted to include backscattering. *Geosci. Model Dev. Discuss.*, 8, 1–48, 2015 www.geosci-
866 model-dev-discuss.net/8/1/2015/ doi:10.5194/gmdd-8-1-2015

867 Proksch, M., Löwe, H., and Schneebeli, M (2015). Density, specific surface area, and correlation
868 length of snow measured by high-resolution penetrometry, *J. Geophys. Res. Earth Surf.*, 120,
869 346–362, doi:10.1002/2014JF003266.

870 Pulliainen J.T., J. Grandell, and M. T. Hallikainen (1999). "HUT snow emission model and its
871 applicability to snow water equivalent retrieval," *IEEE Trans. Geosci. Remote Sens.*, 37(3),
872 1378–1390.

873 Riche F., M Schneebeli and SA Tschanz (2012). Design-based stereology to quantify structural
874 properties of artificial and natural snow using thin sections. *Cold regions science and*

875 | [technology 79, 67-74.](#)

876 Roy A., A. Royer, O. St-Jean-Rondeau, B. Montpetit, G. Picard, A. Mavrovic, N. Marchand, and
877 A. Langlois (2016). Microwave snow emission modeling uncertainties in boreal and subarctic
878 environments, *The Cryosphere*, 10, 623-638, doi:10.5194/tc-10-623-2016.

879 Roy V., K. Goita, A. Royer, A. E. Walker, and B. E. Goodison (2004). “Snow water equivalent
880 retrieval in a Canadian boreal environment from microwave measurements using the HUT
881 snow emission model,” *IEEE Trans.s on Geoscience and Remote Sensing*, 42(9), 1850–1859.

882 Roy, A., Picard, G., Royer, A., Montpetit, B., Dupont, F., Langlois, A., Derksen, C., and
883 Champollion, N. (2013). Brightness Temperature Simulations of the Canadian Seasonal
884 Snowpack Driven by Measurements of the Snow Specific Surface Area, *IEEE T. Geosci.*
885 *Remote*, 51, 4692–4704, doi:10.1109/TGRS.2012.2235842.

886 Rutter, N., Essery, R., Pomeroy, J., Altimir, N., Andreadis, K., Baker, I., Barr, A., Bartlett, P.,
887 Boone, A., Deng, H., Douville, H., Dutra, E., Elder, K., Ellis, C., Feng, X., Gelfan, A.,
888 Goodbody, A., Gusev, Y., Gustafsson, D., Hellström, R., Hirabayashi, Y., Hirota, T., Jonas,
889 T., Koren, V., Kuragina, A., Lettenmaier, D., Li, W.-P., Luce, C., Martin, E., Nasonova, O.,
890 Pumpanen, J., Pyles, R. D., Samuelsson, P., Sandells, M., Schädler, G., Shmakin, A.,
891 Smirnova, T. G., Stähli, M., Stöckli, R., Strasser, U., Su, H., Suzuki, K., Takata, K., Tanaka,
892 K., Thompson, E., Vesala, T., Viterbo, P., Wiltshire, A., Xia, K., Xue, Y., and Yamazaki, T.:
893 Evaluation of forest snow processes models (SnowMIP2), *J. of Geophysical Research:*
894 *Atmospheres*, 114, doi:10.1029/2008JD011063.

895 Rutter N., Sandells, M., Derksen C., Toose P., Royer A., Montpetit B., Langlois A.,
896 Lemmetyinen J., and J. Pulliainen (2014). Snow stratigraphic heterogeneity within ground-
897 based passive microwave radiometer footprints: Implications for emission modeling, *J. of*
898 *Geophysical Research: Earth Surface*, 119, doi:10.1002/2013JF003017.

899 Sandells M., R. Essery, N. Rutter, L. Wake, L. Leppänen, and J.
900 Lemmetyinen (2016). Microstructure representation of snow in coupled snowpack and
901 microwave emission models. *The Cryosphere Discuss.*, doi:10.5194/tc-2016-181.

902 Schwank M., K. Rautiainen, C. Mätzler, M. Stähli, J. Lemmetyinen, J. Pulliainen, J. Vehviläinen,
903 A. Kontu, J. Ikonen, C. Bauduin-Ménard, M. Drusch, A. Wiesmann, and U. Wegmüller
904 (2014). Model for Microwave Emission of a Snow-Covered Ground with Focus on L Band,
905 *Remote Sens. Environ.*, 154, 180-191.

906 Shih, S.-E., Ding, K.-H., Kong, J. A., Yang, Y. E., Davis, R. E., Hardy, J. P., and Jordan, R.
907 (1997). Modeling of millimeter wave backscatter of time-varying snowcover, *Prog.*
908 *Electromagn. Res.*, 16, 305–330.

909 Tedesco M. and E. J. Kim (2006). “Intercomparison of Electromagnetic Models for Passive
910 Microwave Remote Sensing of Snow.” *IEEE Transactions on Geoscience and Remote*
911 *Sensing*, 44(10), 2654–2666.

912 Tsang L., Ding K.-H, Huang S. and Xu X. (2013). Electromagnetic Computation in Scattering of
913 Electromagnetic Waves by Random Rough Surface and Dense Media in Microwave Remote
914 Sensing of Land Surfaces, Invited review paper, *Proc.s of the IEEE TGARS*, 101(2), 255-279.

915 Tsang, L. and Kong, J. A. (2001). *Scattering of electromagnetic waves*, 3, Advanced Topics,
916 Wiley Interscience.

917 Tsang, L., Pan, J., Liang, D., Li, Z., Cline, D. W., and Y. Tan (2007). Modeling active
918 microwave remote sensing of snow using dense media radiative transfer (DMRT) theory with
919 multiple- scattering effects, *IEEE Transactions on Geoscience and Remote Sensing*, 45, 990–
920 1004, doi:10.1109/TGRS.2006.888854.

921 Wegmüller U. and C. Mätzler (1999) “Rough bare soil reflectivity model,” *IEEE Trans. Geosci.*
922 *Remote Sens.*, 37, 3, 1391–1395.

923 Wiesmann A., and C. Mätzler (1999) "Microwave emission model of layered snowpacks",
924 *Remote Sensing of Environment*, 70(3), 307-316.

925 Wiesmann A., C. Mätzler and T. Weise (1998). "Radiometric and structural measurements of
926 snow samples", *Radio Sci.* 33(2), 273-289.

927
928
929

Table 1 Comparison between basics of DMRT-ML/-QMS, MEMLS and HUT-nlayers models. See below for the definitions of terms

Model	DMRT-ML		DMRT-QMS	MEMLS (V3) ^[1]		HUT-nlayers	
Version	V1.6 (with several options)		V 0.1	IBA version	Empirical version	2015	
Physical principle	Maxwell equations + several approximations considering a collection of densely packed sticky spheres			Empirical relationships between micro-structure and scatt/abso/ext coefficients and empirical relation for the dependence of the polarization factors on volume fraction			
Theory	Dense Media Radiative Transfer Model (Shih et al. 1997) (Tsang et al., 2013)			Improved Born Approximation (IBA) ^[2] (Mätzler, 1998)	Empirical scattering coef. (Weismann et al., 1998)	Semi-empirical relation	
Typical range of frequency	1 - 100 GHz						
Approximations Options	Recommended option	Research option	Quasi-Crystalline Approximation (QCA) of Mie scattering	<ul style="list-style-type: none"> • Combination of coherent and incoherent (scattering) reflection between interface layers • Coherence effect for thin ice layer 		<ul style="list-style-type: none"> • Empirical scat. coef. • Semi-empirical absorption coef. 	
	<ul style="list-style-type: none"> • QCA-CP^[3] • Rayleigh assumption • Optional correction for large particles (Grody, 2008) • Mono-disperse sphere radius • No stickiness 	<ul style="list-style-type: none"> • QCA-CP • Rayleigh assumption • No large particles • Poly-disperse (i.e. Rayleigh distribution) • No stickiness 		<ul style="list-style-type: none"> • IBA: option 12 	<ul style="list-style-type: none"> • Different scattering coef.: options 8,10,11 	$\kappa_c(1/m) = \alpha f^2 D_{eff}^{2.8}$ <p>[6]</p>	$\kappa_c(1/m) = \beta (f^4 D_{eff}^6)^{0.2}$ <p>[7]</p>
	<ul style="list-style-type: none"> • Optional stickiness • Optional bubbly ice 			• <u>Optional stickiness</u>	• Ice without air bubble ($p_{ex}=0$)		• Ice as high density snow with $R_{eff}=0$

Model	DMRT-ML	DMRT-QMS	MEMLS (V3) ^[1]	HUT-nlayers
Snow micro-structure parametrization ^[4]	Spheres defined by their radius (R_0) and their stickiness (τ)		Correlation length (p_c or p_{ex}) For 5 to 100 GHz, the model is defined by the correlation length range from 0.05 up to 0.6 mm (Mätzler and Wiesmann, 1999)	Grain geometrical extent (D_{max}) Grain effective diameter ($D_{max,eff}$)
Liquid Water content	Wetness fractional volume of water with respect to ice vol.	No	Volumetric liquid water content W: 0 to about 0.15	Snow moisture (up to several %)
Radiative transfer between layers	DISORT ^[5] (recommended 64 streams or more)	DISORT ^[5] by eigenvalue-quadrature analysis	2 or 6 streams	1 streams (Empirical coef. for forward scatt $q=0.96$)
	Fresnel reflection coef. for snow/snow and snow/atmosphere interfaces			
Main Ref.	Picard et al., 2013 Brucker et al., 2011 Roy et al., 2013 Dupont et al., 2014	Chang et al., 2014 Huang et al., 2012 Liang et al., 2008 Tsang et al., 2007	Proksch et al., 2016 Mätzler and Wiesmann (2014) Wiesmann and Mätzler, 1999 Mätzler and Wiesmann, 1999 Wiesmann et al., 1998 Mätzler 1996, 97, 98, 2004 Schwank et al., 2015	Lemmetyinen et al., 2010a Pulliainen et al., 1999 Kontu and Pulliainen, 2010
Web Site	Open source GPL license http://lgge.osug.fr/~picard/dmrt/ml/	http://web.eecs.umich.edu/~leutsang/Available%20Resources.html	http://www.iapmw.unibe.ch/research/projects/snowtools/memls.html	Upon request

930

931 [1] MEMLS Version 3 (2014) uses updated formulas for the dielectric constants of ice and water. An L-band version of MEMLS was used by
932 Schwank et al. (2015), assuming a simplified one-layer snowpack.

933 [2] IBA: the Improved Born Approximation (IBA) (Mätzler, 1998) expresses the scattering coefficient in terms of the Fourier transform of the
934 two-point correlation function.

935 [3] QCA: The quasi-crystalline approximation (QCA) consists of approximating the resolution of the multiple scattering calculation in a dense
936 porous environment by regarding this medium as a roughly crystalline structure, implying assumptions on the position of two particles
937 between them considered fixed.

938 QCA-CP: QCA can be optionally improved by the so-called Coherent Potential (QCA-CP) (Tsang and Kong, 2001). The basic concept of the
939 CP is to regard the medium near each scatterer as an effective medium with a uniform effective scattering function of aggregates, which
940 implies that the function remains constant in space. The CP approximation thus makes it possible to solve the calculation of the coherent
941 potential Green's operator for multiple scattering (and in the QCA context in our case) assumed as constant in space.

942 [4] See text for the snow microstructure parameterization of each model.

943 [5] The Discrete Ordinate Method (DISORT) is used to numerically solve the radiative transfer equation (Jin, 1994)

944 [6] Extinction coefficient κ_e : $\alpha = 0.000415$, relationship for 18-60 GHz, Hallikainen et al. (1987)

945 [7] Extinction coefficient κ_e : $\beta = 0.461$ Roy et al. (2004)

946

947